Electronic Supplementary Material

A tale of two membranes: from poly(ionic liquid) to metal-organic framework hybrid nanoporous membranes via pseudomorphic replacement

Jian-Ke Sun,[a] Hui-Juan Lin,[a] Wei-Yi Zhang,[a] Min-Rui Gao,[a] Markus Antonietti [a] and Jiayin Yuan*[ab]

[a]Max-Planck-Institute of Colloids and Interfaces, D-14476 Potsdam, Germany. E-mail: jiayin.yuan@mpikg.mpg.de

[b]Department of Chemistry & Biomolecular Science & Center for Advanced Materials Processing (CAMP), Clarkson University, 8 Clarkson Avenue, Potsdam, New York 13699, United States. E-mail: jyuan@clarkson.edu

1. Experimental section

Synthesis of poly(ionic liquid)s. Poly[3-cyanomethyl-1-vinylimidazolium bis(trifluoromethane sulfonyl)imide] (simplified as "PIL") and poly[3-ethyl-1-vinylimidazolium bis(trifluoromethane sulfonyl)imide] (simplified as "PIL-ethyl") were synthesized according to our previous method.[1] The chemical structures were proven by ^{1}H NMR spectra in Figure S1.

Synthesis of porous PIL-OMA membranes

Synthesis of PIL (PIL-BTC) membrane. 50 mg (0.125 mmol of monomer unit) of PIL was dissolved in 1.5 ml of DMF. Subsequently, 8.8 mg (0.042 mmol) of H_3BTC was added and dissolved. The mixture solution was stirred for 3h, before it was cast onto a glass plate. The solvent was evaporated at 80 °C, atmospheric pressure in an oven for 2h. The PIL-BTC film sticking to the glass plate was then immersed into an aqueous solution of 0.25 wt% ammonia for 2 h. The membrane was washed with water for several times and then peeled off from the glass plate for further use.

Synthesis of PIL-ethyl-BTC membrane. The synthetic procedure used above to prepare PIL-BTC membrane was followed using 49 mg (0.125 mmol of monomer unit) PIL-ethyl in place of PIL.

Synthesis of PIL-DOBDC membrane. The synthetic procedure used above to prepare PIL-BTC membrane was followed using 6.2 mg (0.031 mmol) H_4DOBDC (2,5-dihydroxyterephthalic acid) in place of H_3BTC.

Synthesis of PIL-BDC membrane. The synthetic procedure used above to prepare PIL-BTC membrane was followed using 10.4 mg (0.0625 mmol) H_2BDC (benzene-1,4-dicarboxylic acid) in place of H_3BTC.

Synthesis of MOF hybrid membranes

Synthesis of HKUST-1 hybrid membrane. The as-synthesized PIL-BTC membrane was put into 0.1 M $Cu(NO_3)_2$ solution (6 ml) of a DMF-ethanol-water mixture (volume ratio = 1:2:3). The color of membrane gradually turned to green after several hours, yielding the HKUST-1 hybrid membrane after washing by

water and ethanol for several times.

Synthesis of MOF-74-Co hybrid membrane. The as-synthesized PIL-DOBDC membrane was put into 0.1 M $Co(NO_3)_2$ solution (6 ml) of an ethanol-water mixture (volume ratio = 1:1). The color of membrane gradually turned to dark red after one day, yielding MOF-74-Co membrane after washing by water and ethanol for several times.

Synthesis of Cu-BDC hybrid membrane. The as-synthesized PIL-BDC membrane was put into 0.1 M $Cu(NO_3)_2$ solution (6 ml) ethanol-water mixture (volume ratio of 1:1), the color of membrane gradually turned to green after several hours, yielding Cu-BDC membrane after washing by water and ethanol for several times.

Synthesis of HKUST-1 hybrid membrane with PIL-ethyl-BTC membrane as template and precursor. The synthetic procedure used above to prepare HKUST-1 hybrid membrane from PIL-BTC membrane was followed using PIL-ethyl-BTC in place of PIL-BTC.

Direct synthesis of HKUST-1 hybrid membrane from non-porous PIL-BTC membrane. The synthetic procedure used above to prepare HKUST-1 hybrid membrane from porous crosslinked PIL-BTC membrane was followed using PIL-BTC membrane treated by NH_3 gas (so it was crosslinked but without porous structure) in place of a.q.NH_3.

Direct synthesis of HKUST-1 hybrid membrane on the glass substrate without replacement method. 50 mg (0.125 mmol) of PIL was dissolved in 1.5 ml of DMF. Subsequently, 15 mg as-synthesized HKUST-1 crystals was added and dispersed. The solution was stirred for 3h, before it was cast onto a glass plate. The solvent was evaporated at 80 °C, atmospheric pressure in an oven for 2h, which generated the HKUST-1 hybrid membrane on the substrate. It should be mentioned that the obtained membrane is not easily peeled off from the substrate, only the membrane fragment could be obtained by this method.

Growth of HKUST-1 on various substrates

Growth of HKUST-1@carbon paper. 50 mg (0.125 mmol) of PIL was dissolved in 1.5 ml of DMF. Subsequently, 8.8 mg (0.042 mmol) of BTC was added and dissolved. The solution was stirred for 3h, before it was cast onto a carbon paper. The solvent was evaporated at 80 °C, atmospheric pressure in an oven for 2h. The PIL-BTC@carbon paper was then immersed into an aqueous solution of 0.25 wt% ammonia for 2 h. The PIL-BTC@carbon paper membrane was washed with water for several times for further growth of HKUST-1 crystal. The procedure was followed by immersing the PIL-BTC@carbon paper into 0.1 M $Cu(NO_3)_2$ solution (6 ml) of a DMF-ethanol-water mixture (volume ratio of 1:2:3). The color of membrane gradually turned to green after several hours, yielding the HKUST-1@carbon paper superstructure.

Growth of HKUST-1@filter paper. The synthetic procedure used above to prepare HKUST-1@carbon paper was followed using filter paper in place of carbon paper.

Growth of HKUST-1@cotton textile. The synthetic procedure used above to prepare HKUST-1@carbon paper was followed using cotton textile in place of carbon paper.

Growth of HKUST-1@nickel foam. The synthetic procedure used above to prepare HKUST-1@carbon paper was followed using nickel foam in place of carbon paper.

Growth of Janus MOF hybrid membrane HKUST-1@carbon paper@Cu-BDC. The carbon paper was casted with one side by a mixture solution of PIL-BTC. The solvent was evaporated at 80 °C, atmospheric pressure in an oven for 2h. Then the other side of carbon paper was cast a mixture solution of PIL-BDC. The solvent was evaporated at 80 °C, atmospheric pressure in an oven for 2h. The obtained membrane was then immersed into an aqueous solution of 0.25 wt% ammonia for 2 h. The PIL-BTC@carbon paper@PIL-BDC membrane was washed with water for several times, and then it was further immersed in 0.1 M

$Cu(NO_3)_2$ solution (6 ml) of an ethanol-water mixture (volume ratio of 1:1), yielding HKUST-1@carbon paper@Cu-BDC Janus MOF hybrid membrane.

NH_3 gas driven actuation. A piece of HKUST-1 hybrid membrane strip (11 mm × 2 mm × 38 μm) was placed into NH_3 gas (T = 20 ^oC, 857 kPa); the NH_3 triggered the fast bending movement of the membrane. Afterwards, the membrane was taken out and heated at 80 ^oC in air to accomplish the shape recovery. For the sensing test of membrane actuator, the as-synthesized HKUST-1 hybrid membrane was directly placed into the NH_3 gas of different volume concentrations (vol%) in air atmosphere.

HKUST-1 polycrystalline sample swelling in NH_3 atmosphere. The as-synthesized HKUST-1 polycrystalline sample (45 mg) was ground into a powder and added into a glass tube (Φ = 5 mm). This tube was caped with one needle for gas inlet and another needle for gas outlet. The NH_3 gas was slowly injected into the tube to flush the HKUST-1 crystal in NH_3 bath. For comparison, the air was injected into a tube containing the HKUST-1 polycrystalline sample under the same condition. Images of samples were taken at ambient temperature.

Characterization methods.

All chemicals were from commercial sources and used without further purification.

N_2 sorption analysis was performed at 77 K on a QUADROSORB SI, equipped with automated surface area and pore size analyzer. Before analysis, samples were degassed at 150 ^oC for 12 h using a masterprep degassing system. The CO_2 sorption isotherms were measured at 273 K, using the same device to N_2 sorption analysis. The porosity of meso- and macropore and the pore size distributions of the membrane were measured by a mercury intrusion porosimetry for meso- and macropore analysis with an Autopore III device (Micromeritics,

USA) according to DIN 66133 at Federal Institute for Materials Research and Testing (BAM), Berlin. The morphology of the membranes was visualized using a Gemini scanning electron microscope (SEM) under 3 kV (acceleration voltage). Energy-dispersive X-ray (EDX) mapping and analysis were taken on the SEM with an EDX spectrometer. X-Ray powder diffraction (XRD) patterns were recorded on a Bruker D8 diffractometer equipped with scintillation counter. X-ray photoelectron spectroscopy (XPS) studies were performed with a ThermoFisher ESCALAB250 X-ray photoelectron spectrometer (powered at 150 W) using Al Kα radiation (λ = 8.357 Å). To compensate for surface charging effects, all XPS spectra were referenced to the C 1s neutral carbon peak at 284.6 eV. The solution UV-Vis absorption measurements were recorded on a Lambda 900 spectrophotometer. The solid UV-Vis diffuse reflectance spectra were recorded using a Lambda 950 spectrophotometer with $BaSO_4$ as a reference. ^{1}H nuclear magnetic resonance (^{1}H-NMR) measurements were carried out at room temperature on a Bruker DPX-400 spectrometer. Fourier transform infrared spectroscopy (FT-IR) spectra were accomplished on a BioRad 6000 FT-IR spectrometer, samples were measured in solid states using a Single Reflection Diamond ATR. The total amount of copper in HKUST-1 hybrid membrane was determined by inductively coupled plasma optical emission spectrophotometer (ICP-OES), and the measurement was performed on a Perkin Elmer Optima 8000, calibrated with standard solutions.

2. Additional data and figures

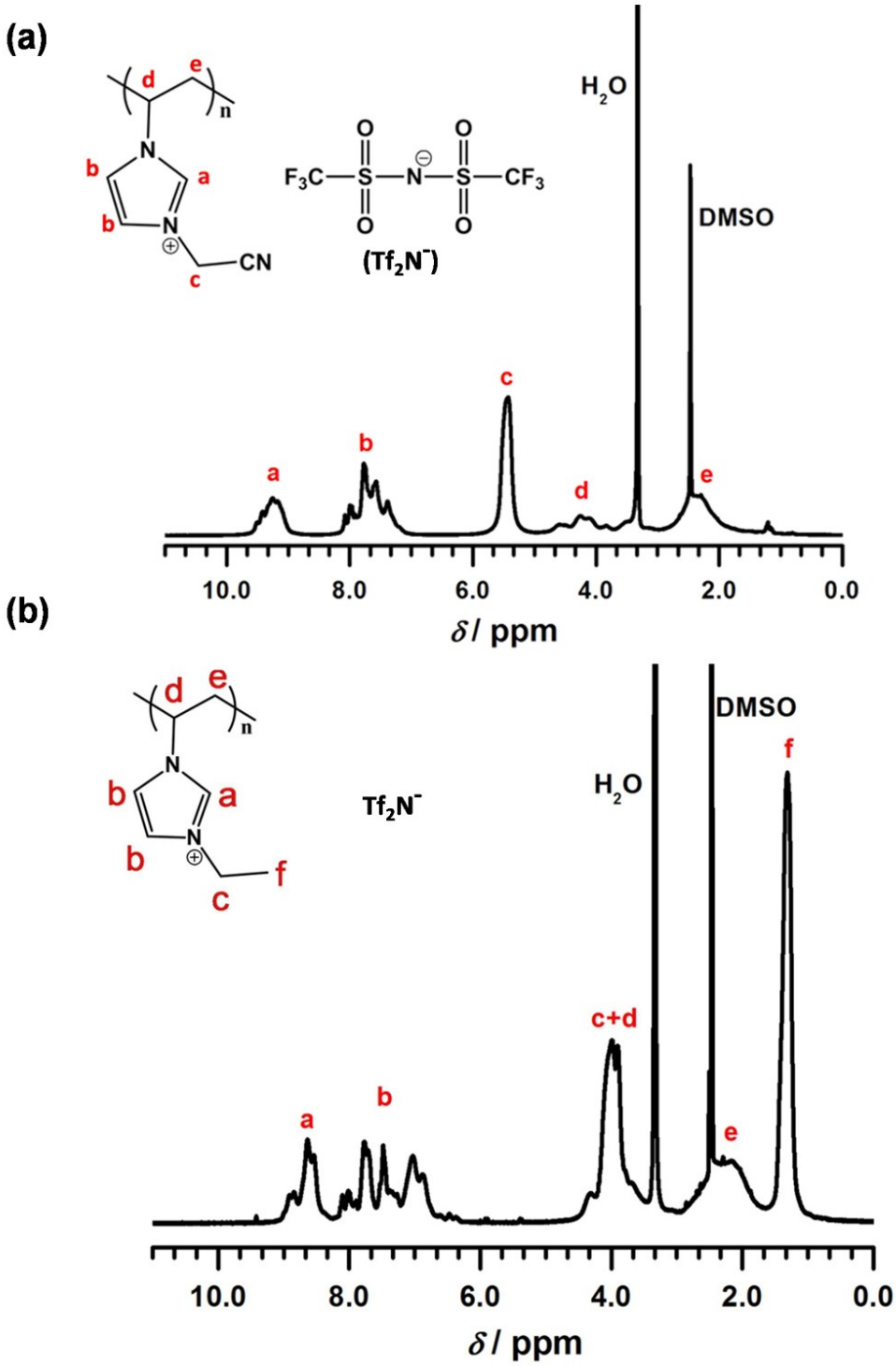

Figure S1. Chemical structures and [1]H-NMR spectra of PILs employed in the text. (a) poly[3-cyanomethyl-1-vinylimidazolium bis(trifluoromethane sulfonyl)imide] (PIL) and (b) poly[3-ethyl-1-vinylimidazolium bis(trifluoromethane sulfonyl)imide] (PIL-ethyl). The spectra matched that reported in our previous literature.[1]

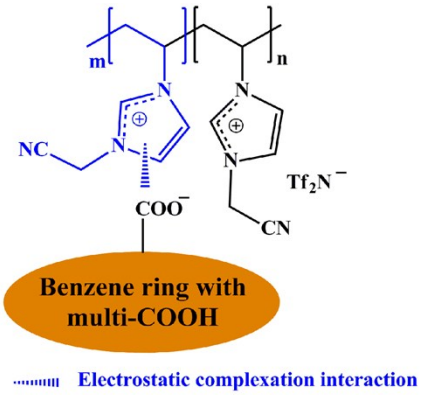

Figure S2. Scheme of determination of the DEC (degree of electrostatic complexation) of PIL membrane from **Ref 2**. DEC= m/(m+n). m denotes the number of crosslinked imidazolium units and n is the number of uncrosslinked units. Sulfur, which is only present in the Tf_2N^- counteranion in the PIL is replaced by the carboxylate of the acid during the ionic complexation. Therefore, the sulfur content is a reliable measure of local ionic complexation inside the membrane. EDX analysis of sulfur was used in order to determine the amount of Tf_2N^- counteranion which is directly related to the amount of non-cross-linked imidazolium units. As mentioned in our previous work, a gradual increase in the amount of sulfur from the top to the bottom was observed (it is the same in the current membrane, the amount of sulfur from the top (0.55 wt%) to the bottom (13.59 wt%) increase as evidenced by EDX analysis), which is characteristic for a gradual drop in the DEC, *i.e.* the relative portion of the imidazolium unit along the PIL chain in a cross-linked network decreased.

Function of NH_3 in the porous PIL membrane fabrication

To fabricate porous PIL membranes, the PIL and H_3BTC are mixed first in DMF. In DMF, H_3BTC is protonated and noncharged, thus is molecularly mixed with PIL in DMF. Upon solution casting onto a glass plate, a PIL/H_3BTC blend film forms and sticks to the glass plate. When the glass place is immersed in aqueous NH_3 solution, NH_3 will diffuse into the blend film, and neutralizes H_3BTC into anionic BTC^{3-}. The newly formed BTC^{3-} due to its multivalency preferentially complexes with the cationic PIL, thus forming a crosslinked network. Thus, NH_3 is the trigger for the crosslinking reaction.

Pore formation mechanism

The pore formation process is intrinsically related to the unique properties the PIL. The used PIL is a polycation and hydrophobic. When the PIL/H_3BTC blend film is immersed into aqueous NH_3 solution, both NH_3 and water molecules start to diffuse into the blend film. The consequence of NH_3 diffusion has been explained above, that is, to form a crosslinking network. Meanwhile upon the diffusion of water into the blend film, phase separation due to the hydrophobic nature of the PIL takes place. It is well-known that phase separation is a classic way to produce porous membranes. Since diffusion of NH_3 and water molecules into the blend film starts simultaneously, the phase separation and crosslinking reaction run side by side, that is, once the pore is formed by the phase separation process, it will be immediately stabilized by the crosslinking process.

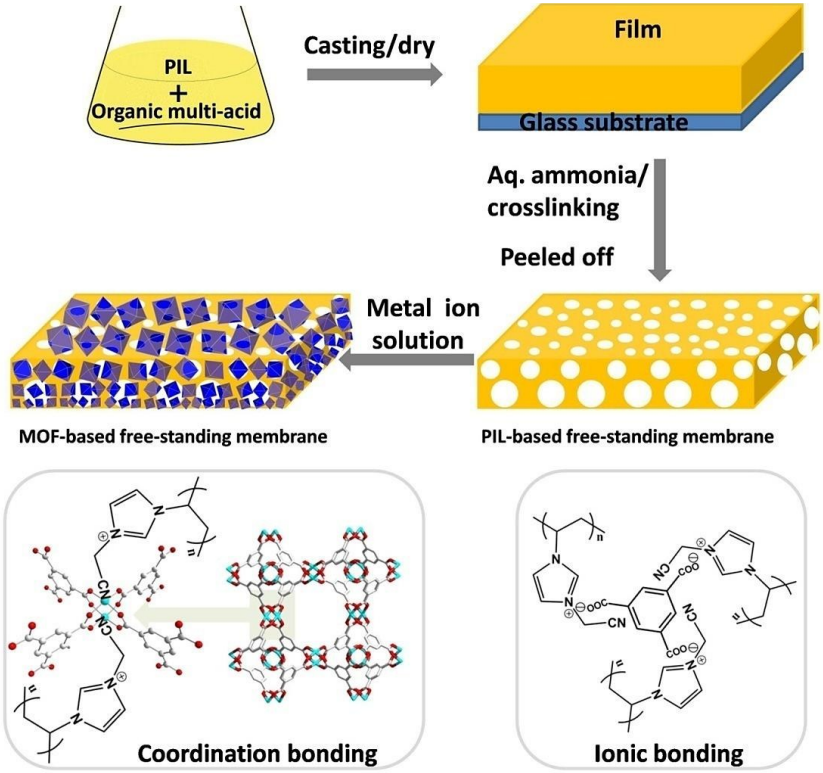

Figure S3. Schematic illustration of the process of preparing free-standing MOF hybrid membrane via pseudomorphic replacement approach. The corresponding chemical structures are shown at the bottom to illustrate the equilibrium transformation by cutting ionic bond and subsequent formation of coordination bond. The HKUST-1 crystal structure as a prototypical MOF is presented here (carbon atom: gray; oxygen atom: red; copper atom: turquiose).

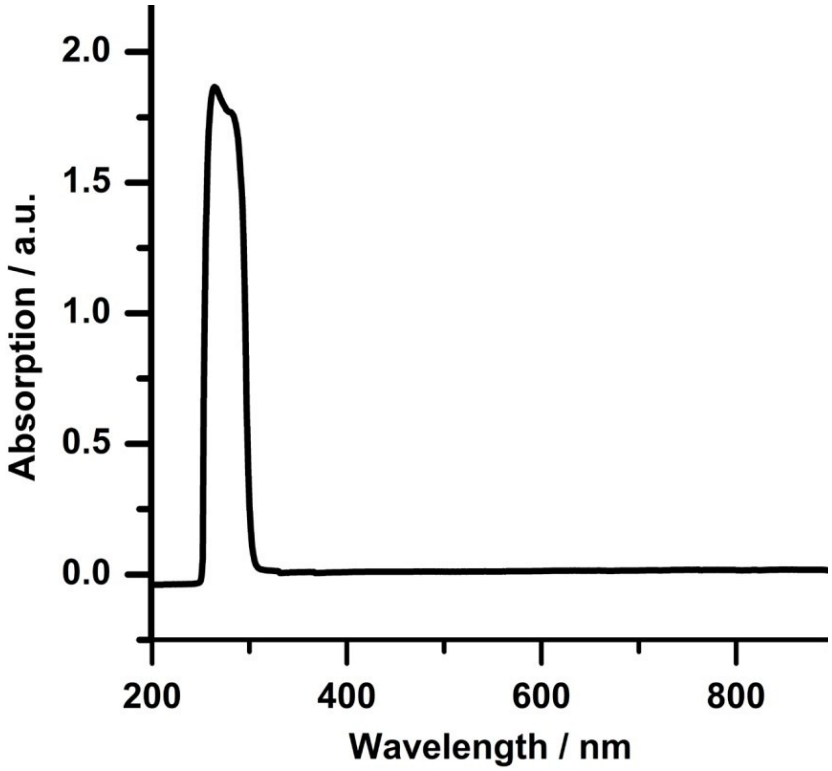

Figure S4. The UV-vis spectrum of H_3BTC solution (6 ml) in DMF/ethanol/water (volume ratio = 1:2:3) mixture.

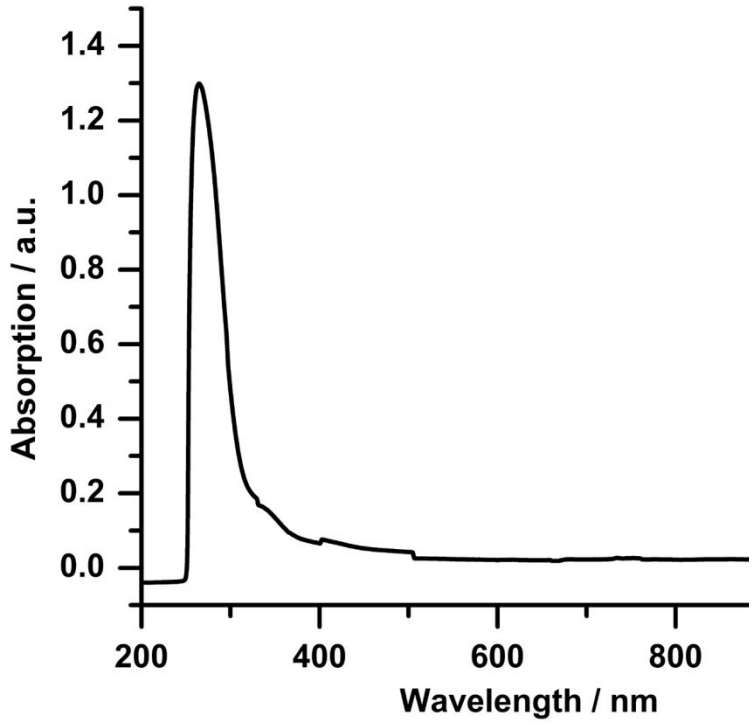

Figure S5. The UV-vis spectrum of PIL solution (6 ml) in DMF/ethanol/water (volume ratio = 1:2:3) mixture.

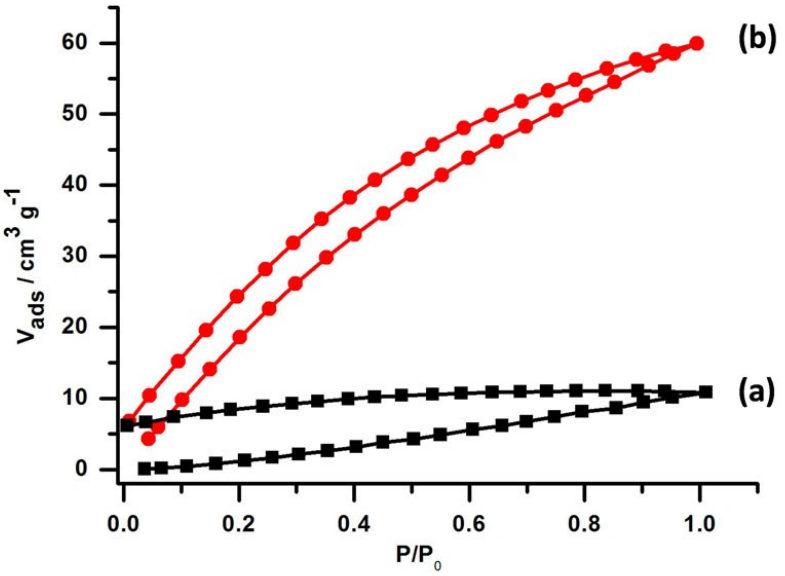

Figure S6. The sorption isotherms of CO_2 at 273 K. (a) PIL membrane and (b) HKUST-1 hybrid membrane.

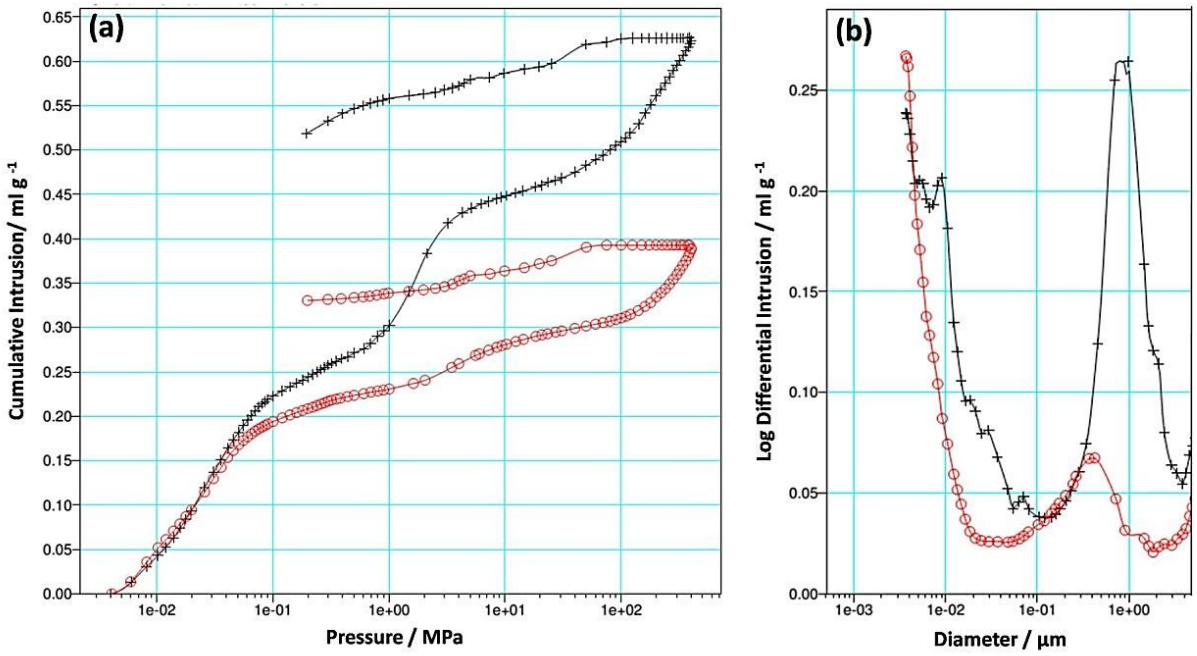

Figure S7. Results of porosity studies of PIL membrane (dark) and HKUST-1 hybrid membrane (red) by mercury intrusion. (a) Cumulative volume of mercury versus pressure. (b) Pore size distribution curve of the corresponding membranes.

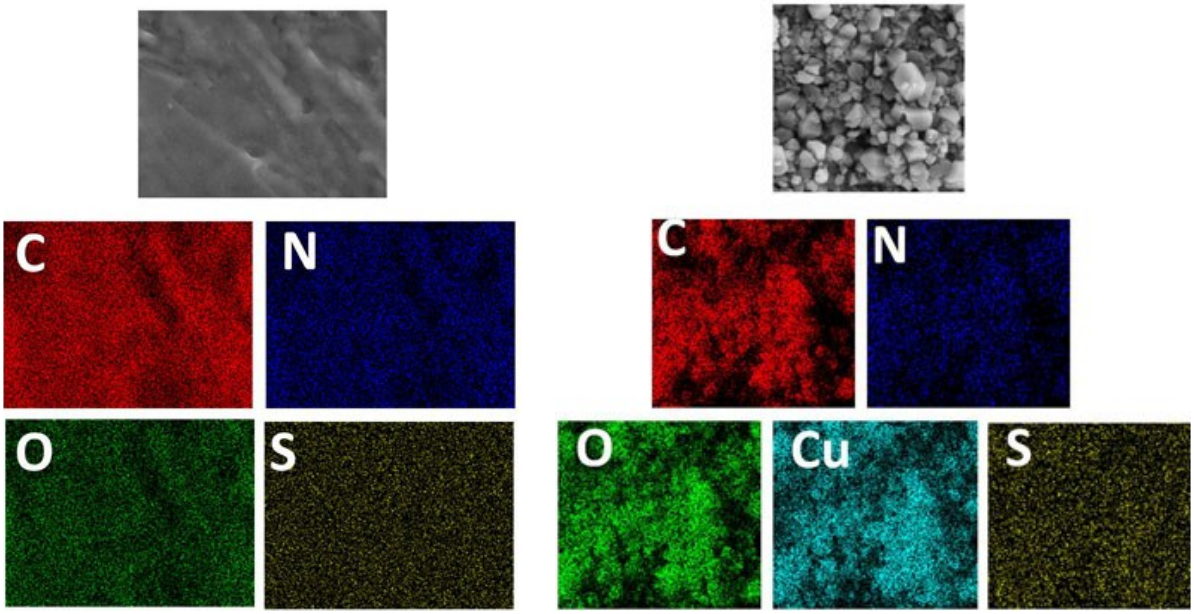

Figure S8. The EDX mapping of membrane. Top surface of PIL membrane (left) and HKUST-1 hybrid membrane (right). Cu signal was absent in the PIL membrane.

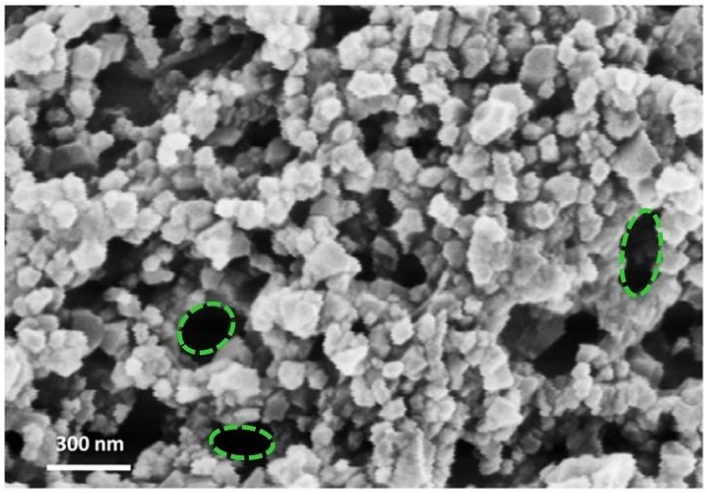

Figure S9. SEM image of HKUST-1 crystal morphology at the bottom side of HKUST-1 hybrid membrane. The pores (green circle) of original PIL membrane still could be observed, which demonstrated the well-maintained integrity of the original porous PIL membrane after the replacement process.

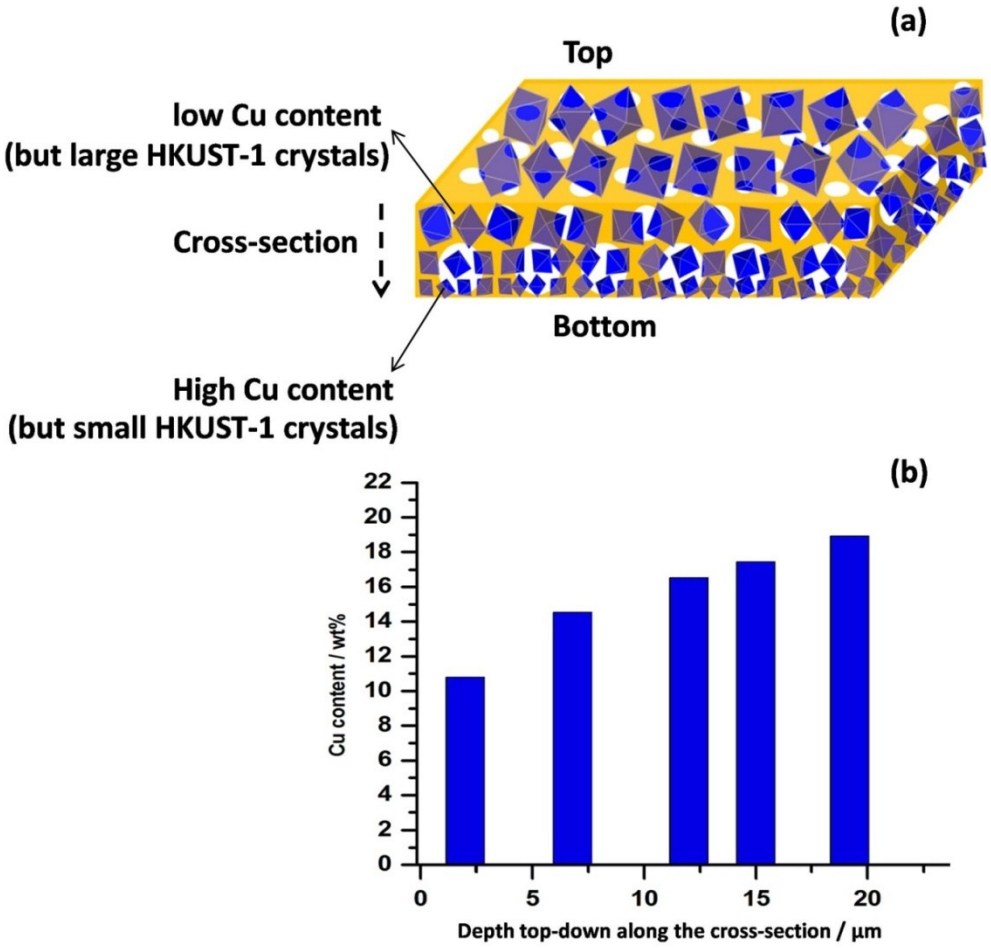

Figure S10. Characterization of cross-section of HKUST-1 hybrid membrane by EDX analysis. (a) A scheme showing the gradient Cu mass content by EDX analysis. A HKUST-1 hybrid membrane (thickness ca. 20 µm) was prepared and the elemental composition at different positions along the membrane cross-section (indicated by dashed arrow) was analyzed by means of EDX analysis. (b) Cu element content at different depth from top to bottom along the cross-section of the HKUST-1 hybrid membrane. An increasing gradient in Cu mass content from top to bottom is obviously observed.

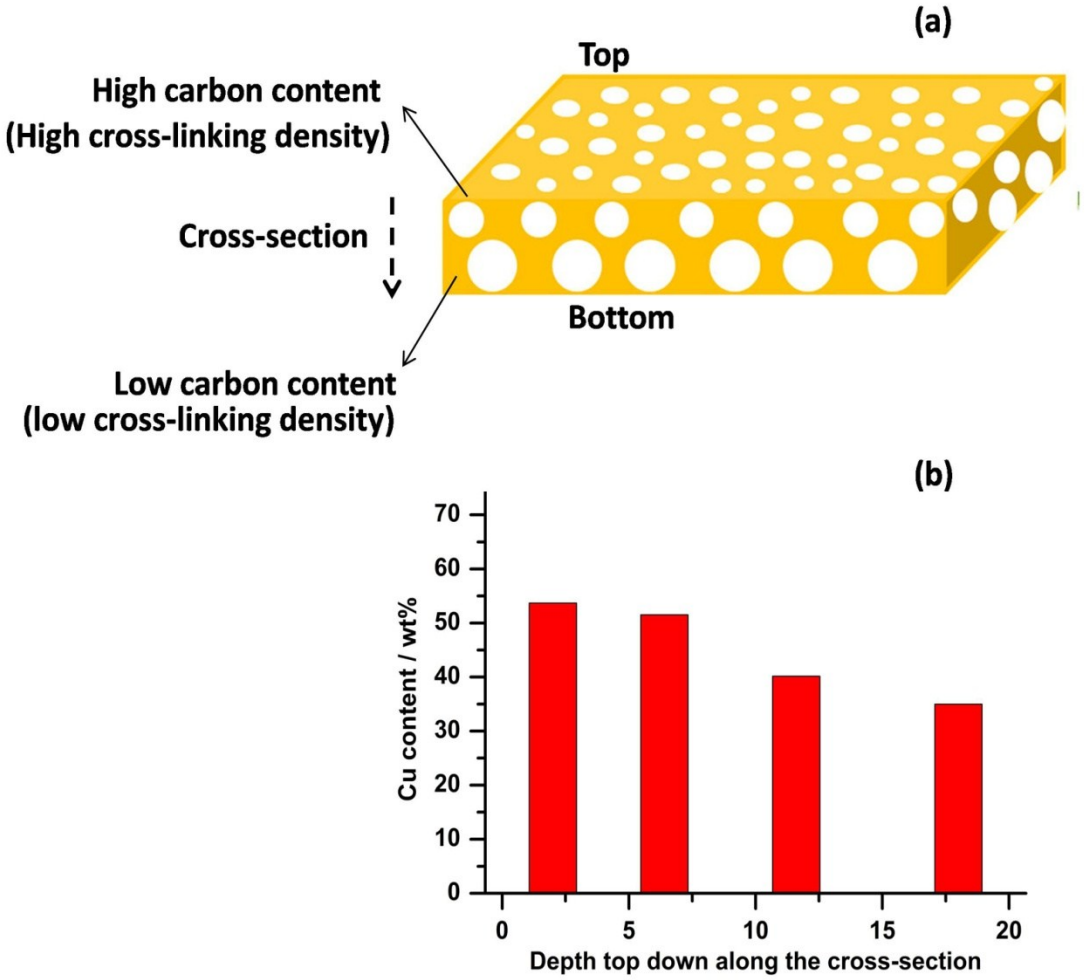

Figure S11. Characterization of cross-section of PIL membrane by EDX analysis. (a) A scheme showing the gradient carbon mass content by EDX analysis. A PIL membrane (thickness ca. 22 μm) was prepared and the elemental composition (4 positions) along the membrane cross-section (indicated by dashed arrow) was analyzed by means of EDX analysis. (b) Carbon element content at different depth from top to bottom along the cross-section of PIL membrane.

The reason behind the stepwise decrease of carbon content is caused by release of H_3BTC into ammonia solution. That is, the more H_3BTC is lost, the higher the carbon concentration is. From Figure S11b, it is clear that H_3BTC is of lower concentration on the top, which increases gradually to the bottom. The loss of H_3BTC occurred when the PIL-trimesic acid blend film was immersed in aqueous ammonia solution, during which some H_3BTC on the top were neutralized by ammonia to enter aqueous solution without complexation with the PIL (see the analysis below).

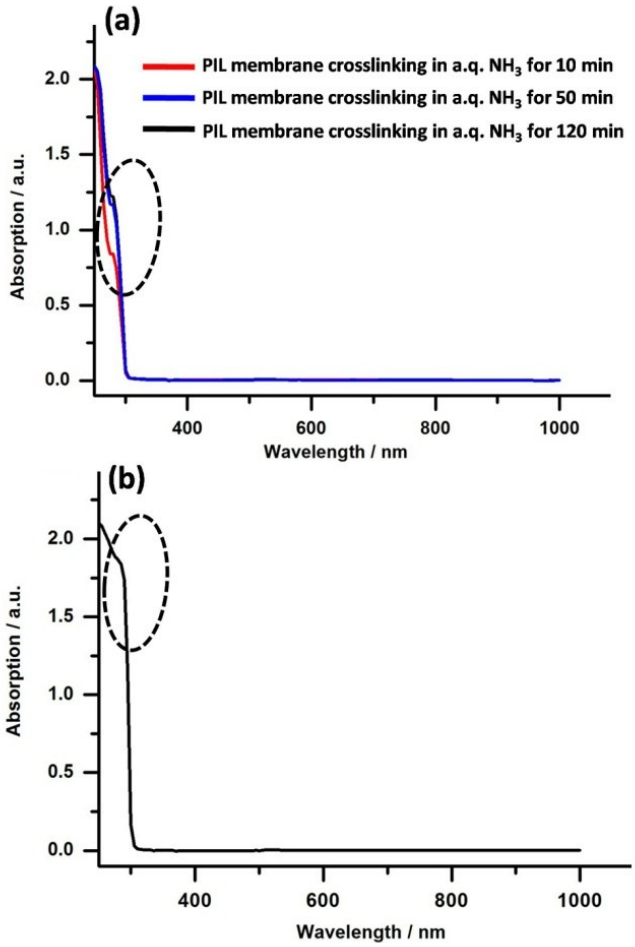

Figure S12. UV-Vis absorption characterization of (a) the a.q NH_3 solution (0.25 wt%) during the formation of porous PIL membrane at different time intervals. Time zero is the moment when the PIL/ H_3BTC blend film was immersed in ammonia solution. (b) The a.q NH_3 solution (0.25 wt%) when only the same amount of H_3BTC (8.8 mg) was added to the ammonia solution. Note: the protonated H_3BTC is not soluble but deprontated BTC^{3-} is soluble.

From the UV-Vis spectra of (a), a quick release of H_3BTC into a.q NH_3 solution during the porous PIL membrane formation process was observed, as revealed by the appearance of the characteristic absorption of BTC^{3-} in solution (peak: 280 nm) after 10 min. The release of H_3BTC into solution stopped after 2h, when the development of the PIL porous polymer was completed. Therefore a part of H_3BTC in top membrane part must be neutralized very rapidly and was released into solution. This process is responsible for a gradient of carbon content along the membrane cross-section from top to bottom, as discussed in Figure S11.

The amount of H_3BTC release to the a.q. NH_3 solution could be quantitatively calculated by comparing the intensity at 280 nm, which is around 35 % BTC in the PIL membrane. This value is in good accordance with the ICP analysis of Cu in the MOF hybrid membrane, which found a weight ratio of Cu and BTC (0.45:1) in HKUST-1 hybrid membrane. This ratio is very close to the theoretical ratio (0.46:1) in $Cu_3(BTC)_2$ molecule, demonstrating that the more than 95% of BTC in the HKUST-1 hybrid membrane

coordinates with Cu^{2+} ion.

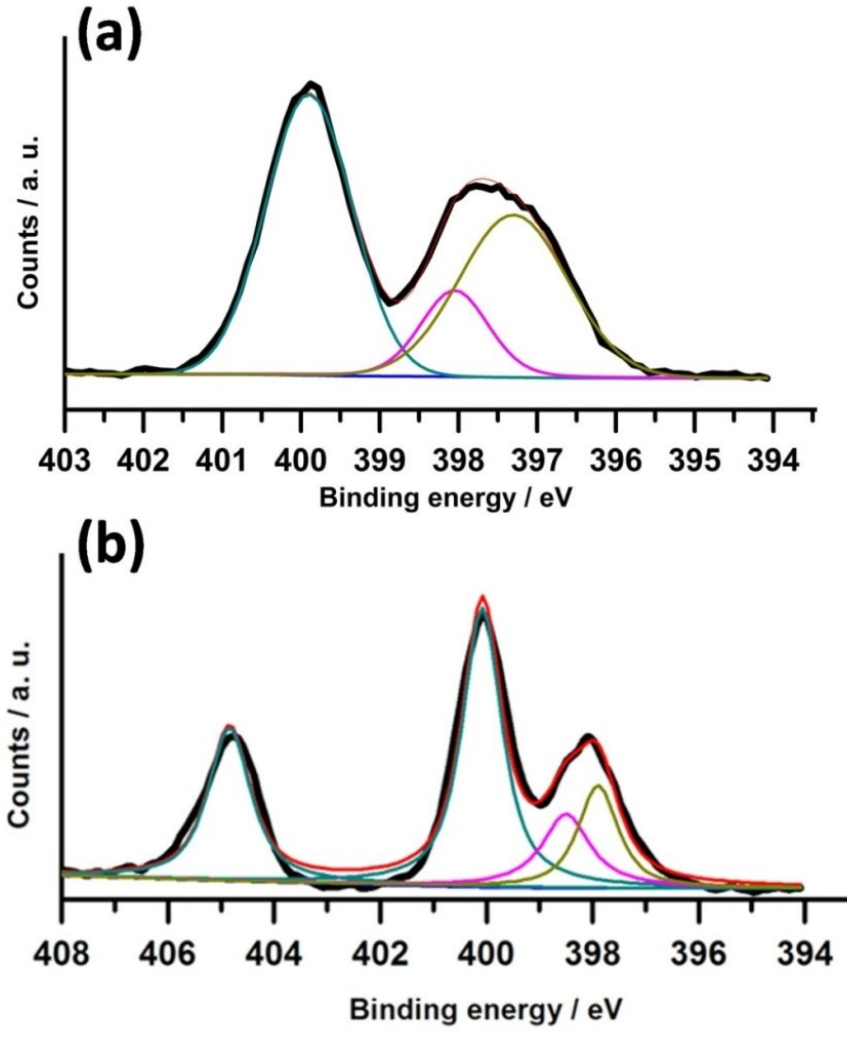

Figure S13. XPS spectra for N 1s signals in (a) PIL and (b) Cu(II)-PIL mixture. The N 1s core-level spectrum of PIL can be fitted by three well-resolved components at 399.9, 398.0 and 397.3 eV, which are ascribed to the N atoms of imidazolium cation rings, the cyano group and $TSFI^-$ anion, respectively. As for the Cu(II)-PIL mixture, the N 1s core-level spectrum can be fitted by four well-resolved components at 404.8, 400.1, 398.5 and 397.9 eV, which are ascribed to the N atoms of NO_3^- anion, the imidazolium cation rings, the cyano group and $TSFI^-$ anion, respectively. Compared with the peak of cyano group N atoms (398.0 eV) in PIL, the obvious shift (0. 5 eV) of corresponding peak to high binding energy positions was detected in Cu(II)-PIL (398.5 eV), This observations indicate an charge transfer process from cyano group to Cu(II) in Cu(II)-PIL mixture.

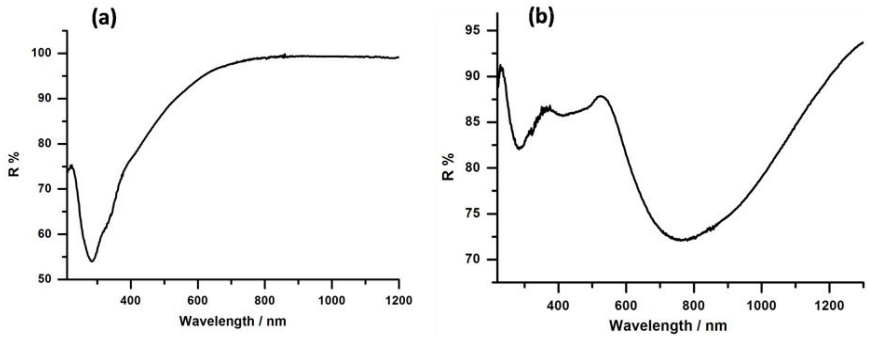

Figure S14. Solid UV-vis spectra characterization. UV-vis diffuse reflectance spectra of (a) PIL membrane and (b) HKUST-1 hybrid membrane. In addition to the appearance of characteristic broad absorption of HKUST-1 phase between 600 and 1300 nm, another obvious absorption in range of 400-550 nm could be observed. Such absorption could be attributed to the ligand to metal charge transfer (LMCT) transitions from cyano group to Cu (II) ions due to coordination binding interaction, as it is consistent with previous literature.[3]

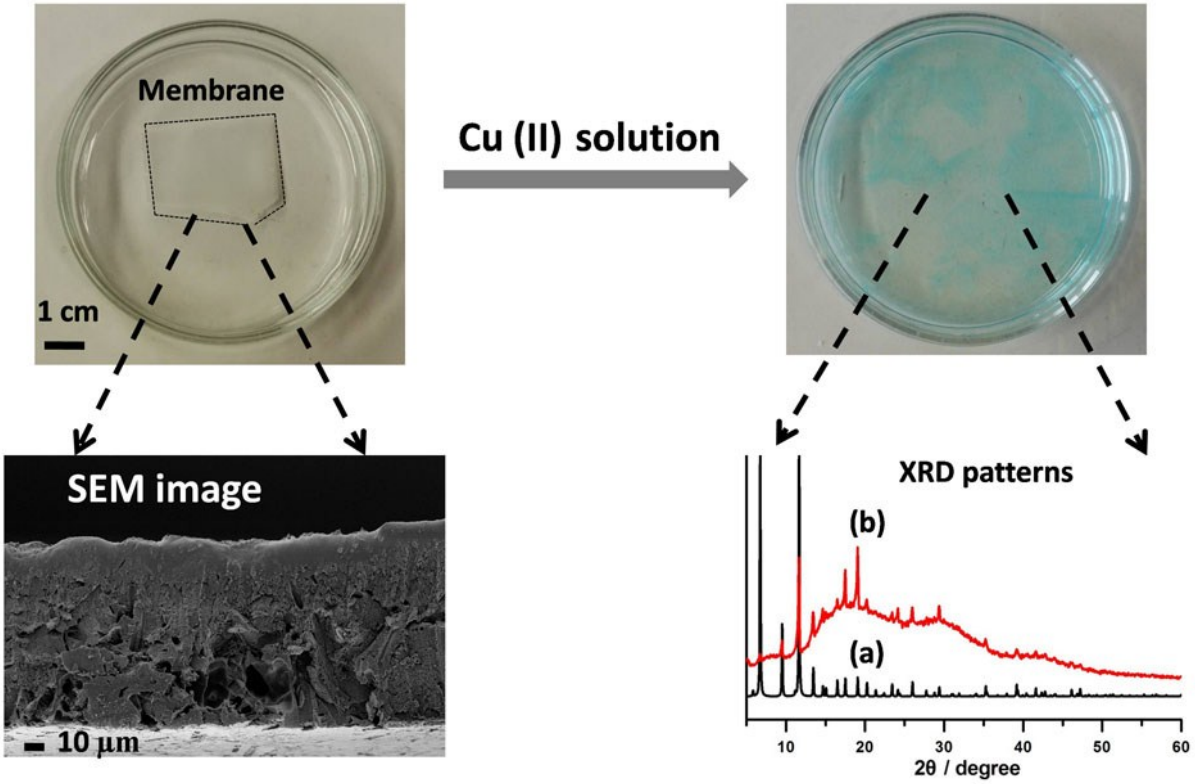

Figure S15. Using PIL-ethyl membrane for HKUST-1 hybrid membrane fabrication. The replacement process by using PIL-ethyl membrane as the template and precursor (left glass dish, the edge of membrane was highlighted by dotted line for clarity). The degradation of the membrane was observed as the small green cracks formed after immersing the origin PIL-ethyl membrane in Cu(II) solution (right glass dish). The XRD patterns demonstrated that the formed green cracks (right glass dish) contained HKUST-1 phase

(b), as it is consistent with the simulation from single crystal data of HKUST-1(a).

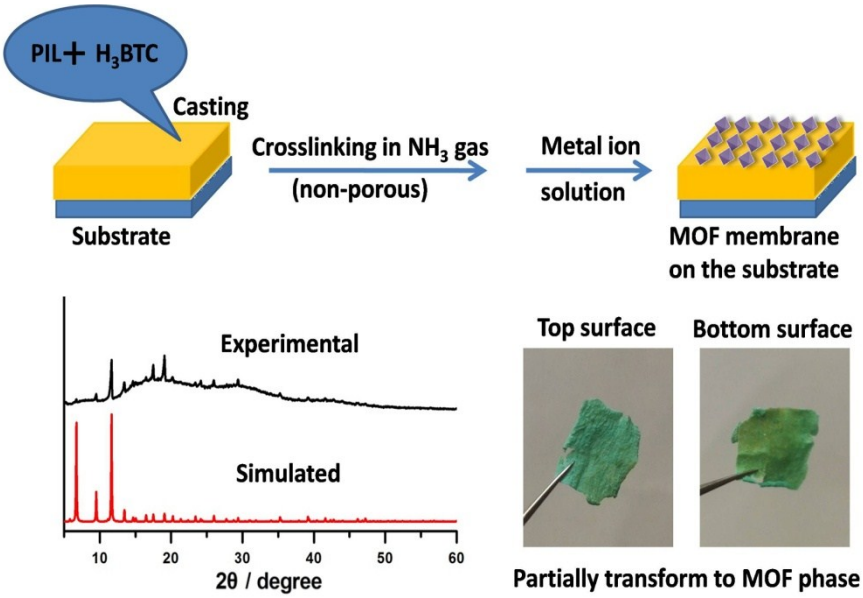

Figure S16. The control experiment by using nonporous PIL membrane as the template and precursor for preparing HKUST-1 hybrid membrane. Although the formation of HKUST-1 phase was demonstrated by XRD pattern, the membrane was not evenly replicated as detected from the nonuniform color of membrane fragment on both top and bottom surfaces. Reasonably, the lack of the pore of precursor membrane can't provide the channel for metal ion diffusion from top to bottom part.

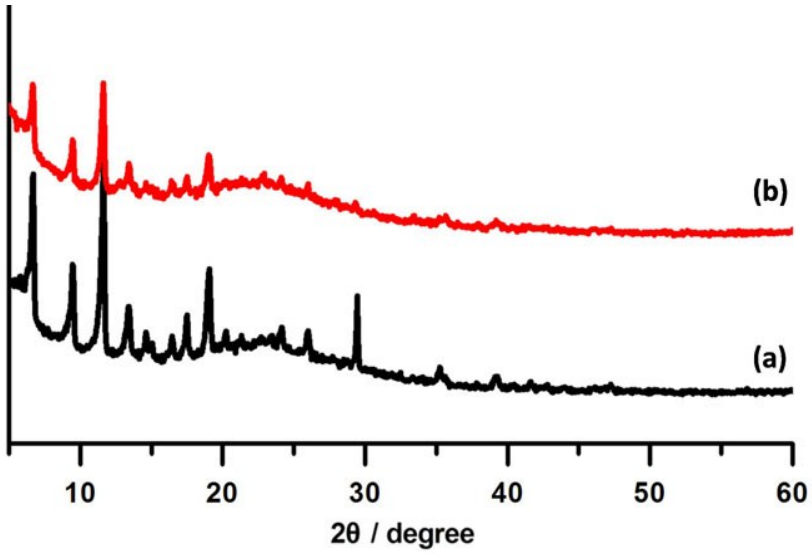

Figure S17. XRD characterization to study the stability of HKUST-1 hybrid membrane in DMF solution. (a) the as-synthesized HKUST-1 hybrid membrane and (b) after storage of the HKUST-1 hybrid membrane in DMF solution for one week. No observable degradation of membrane was detected in solution, and the XRD pattern of membrane was consistent with the origin HKUST-1 hybrid membrane. These data

demonstrate the strong glue effect of PIL chains toward binding the HKUST-1 crystals to maintain the integrity of membrane.

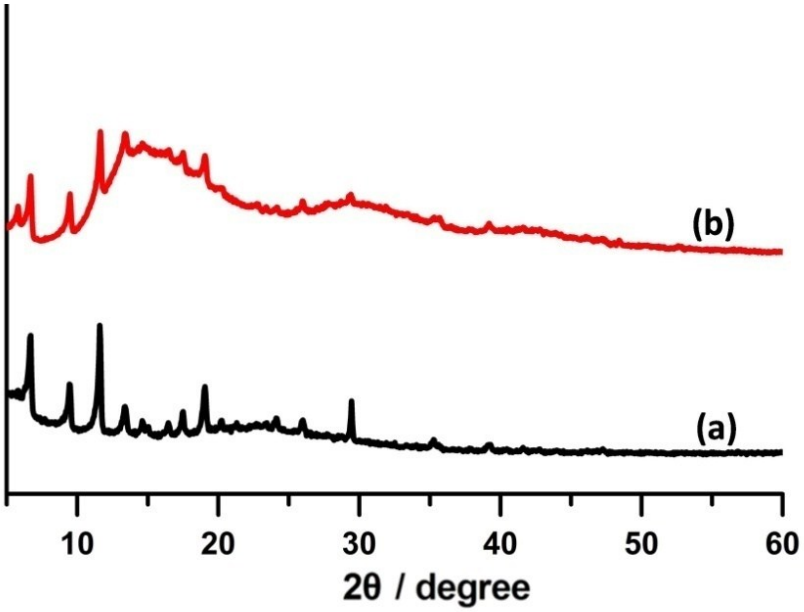

Figure S18. XRD characterization to study the stability of HKUST-1 hybrid membrane in air. (a) the as-synthesized HKUST-1 hybrid membrane and (b) after being in air (relative humidity: 20~30 %) for two months.

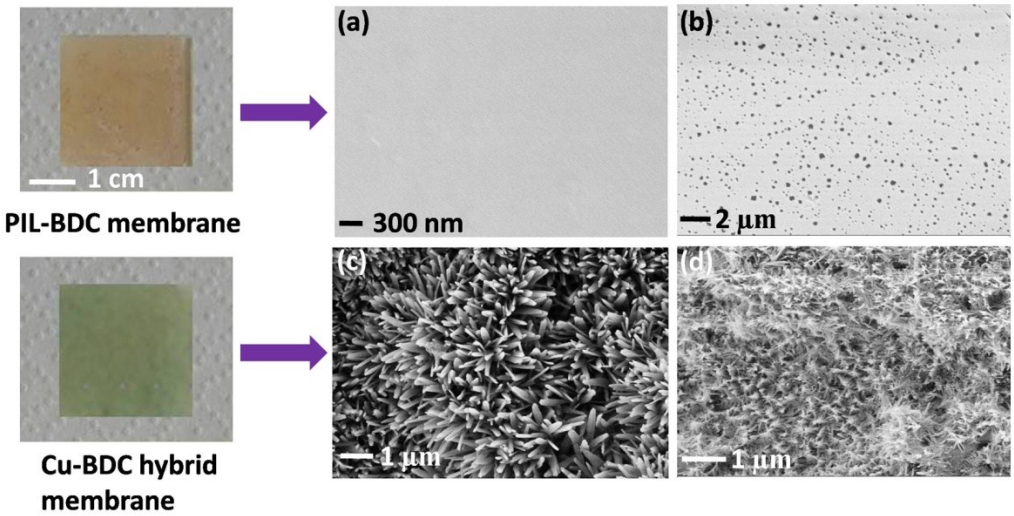

Figure S19. The preparation of Cu-BDC hybrid membrane via the replacement of PIL-BDC hybrid membrane. The corresponding photographs (left) and SEM images (right) of morphology of each membrane. (a) Top surface and (b) bottom surface of PIL-BDC hybrid membrane. (c) Top surface and (d) bottom surface of Cu-BDC hybrid membrane.

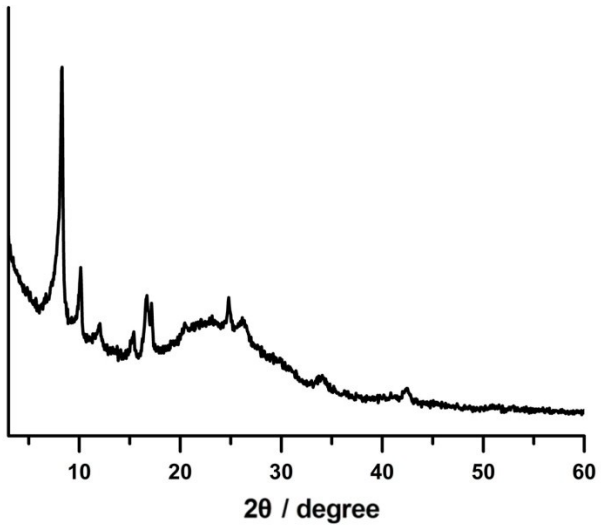

Figure S20. The XRD pattern of Cu-BDC hybrid membrane. It should be mentioned that a downshift of peaks was observed in the Cu-BDC hybrid membrane in comparison with directly synthesized Cu-BDC crystalline phase in solution.[4] Such behavior was attributed to the solvent effect on the metal site, which have been revealed by previous work.[4-6]

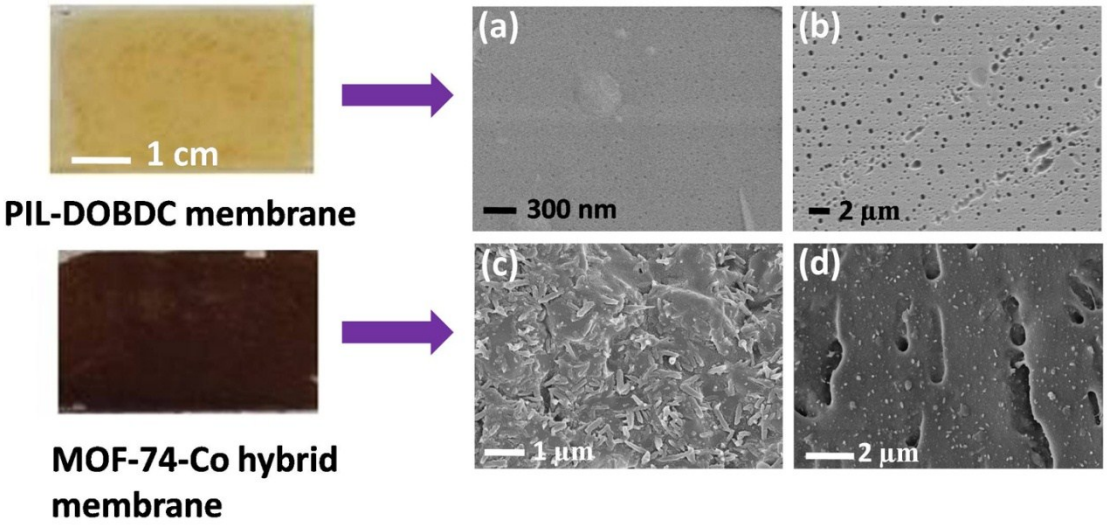

Figure S21. The preparation of MOF-74-Co hybrid membrane via the replacement of PIL-DOBDC hybrid membrane. The corresponding photographs (left) and SEM images (right) of morphology of each membrane. (a) Top surface and (b) bottom surface of PIL-DOBDC hybrid membrane. (c) Top surface and (d) bottom surface of MOF-74-Co hybrid membrane.

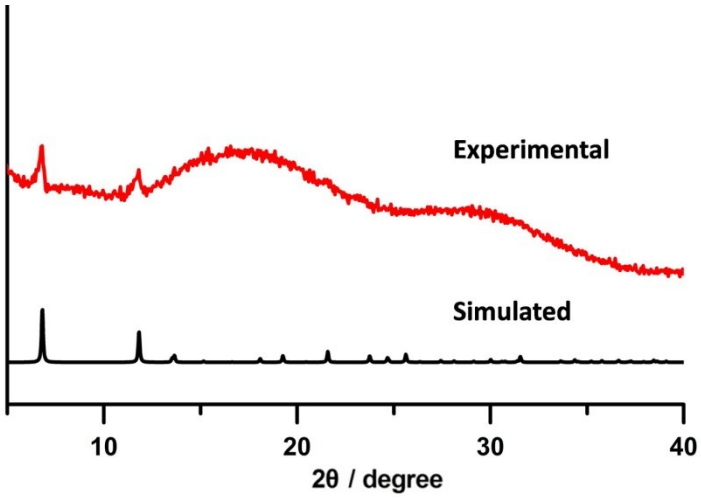

Figure S22. The XRD pattern of MOF-74-Co hybrid membrane. The plot was consistent with the simulation from single crystal data.

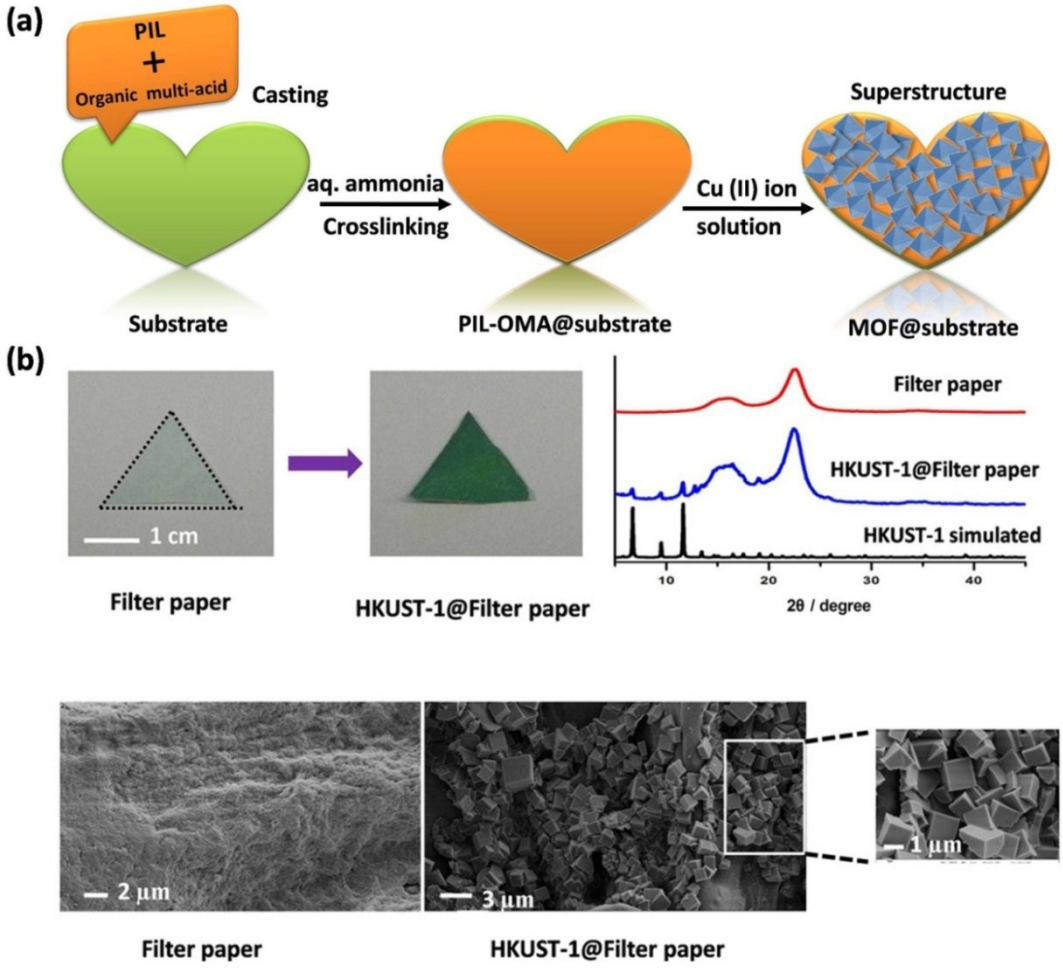

Figure S23. The growth of MOF superstructures on substrate. (a) Schematic illustration of general procedure toward preparation of free-standing MOF superstructure combined with various substrates by PIL-assisted replacement approach. (b) The growth of HKUST-1 on the filter paper. Successful positioning of MOF phase on substrate was demonstrated by XRD and SEM characterizations.

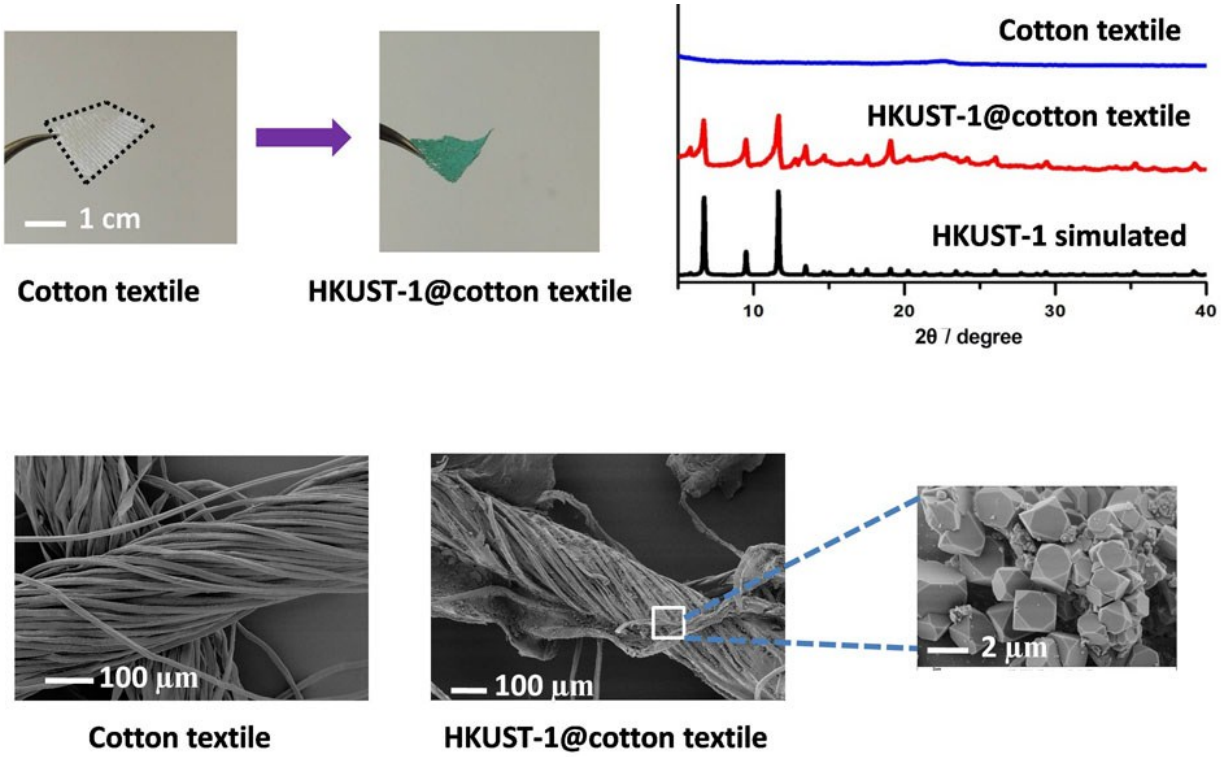

Figure S24. The growth of HKUST-1 on cotton textile. The successful positioning of the MOF phase on substrate was demonstrated by XRD and SEM characterizations.

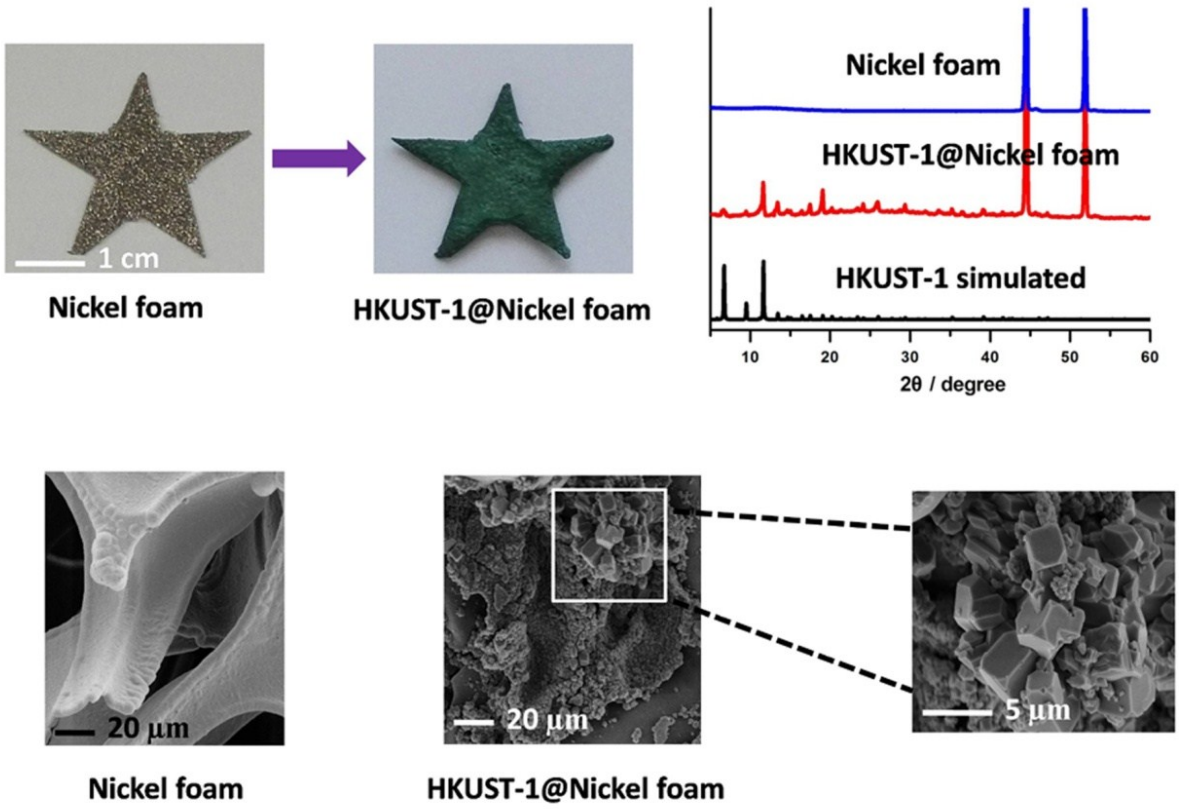

Figure S25. The growth of HKUST-1 on the nickel foam. The successful positioning of the MOF phase on substrate was demonstrated by XRD and SEM characterizations.

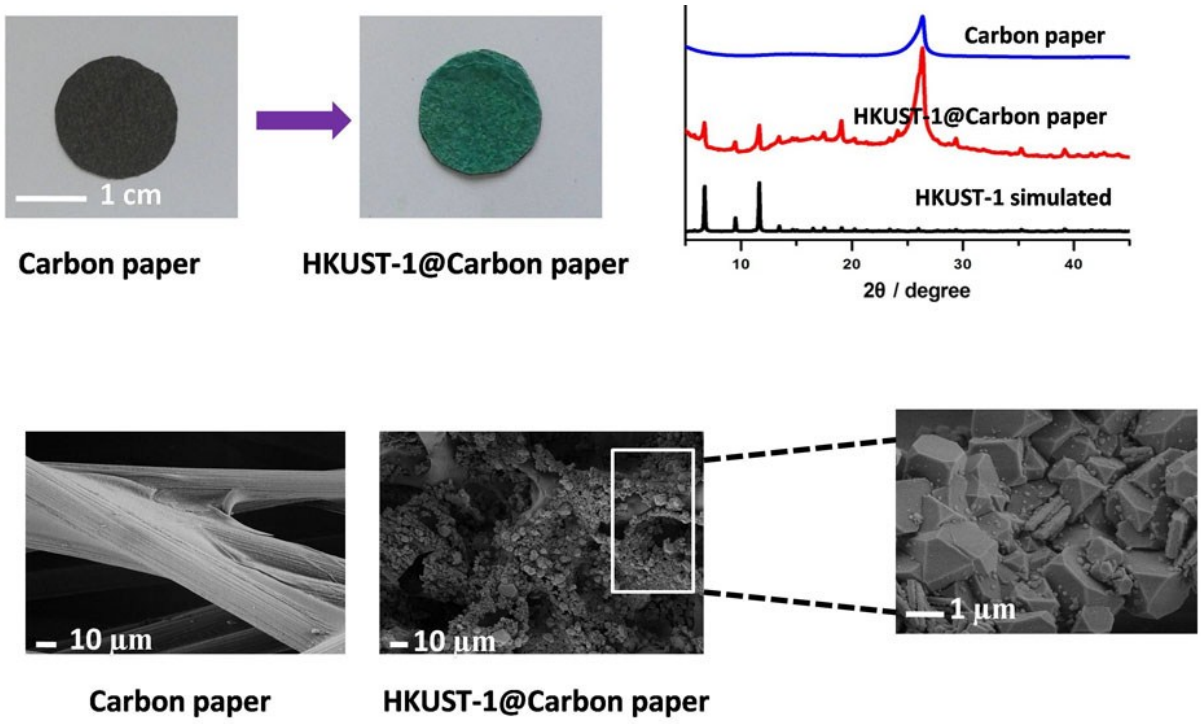

Figure S26. The growth of HKUST-1 on the carbon paper. The successful positioning of the MOF phase on substrate was demonstrated by XRD and SEM characterizations.

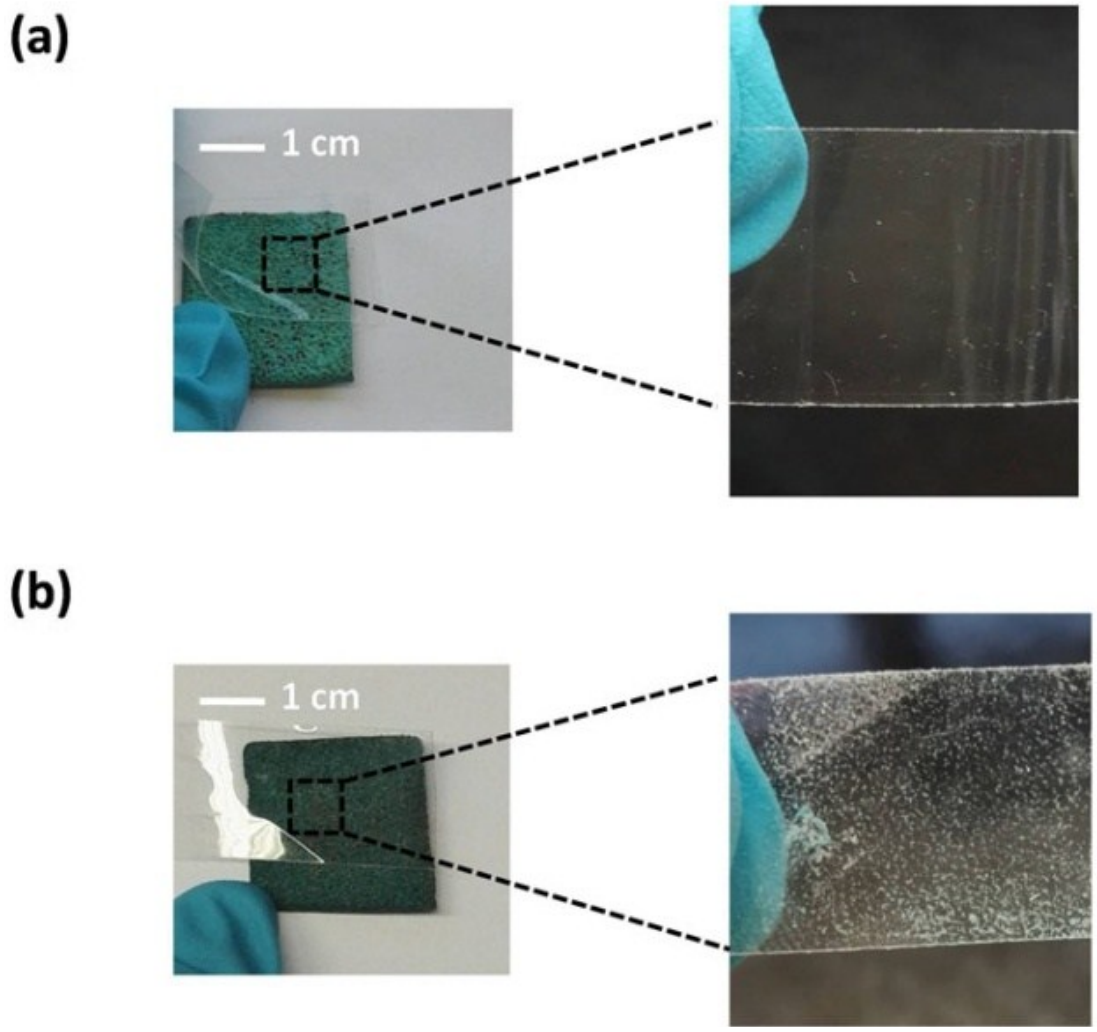

Figure S27. Abrasion resistance tests performed through adhesion with adhesive tape. (a) left: photograph of the HKUST-1 growth on nickel foam through PIL-assisted replacement method; right: photograph of a tape after abrasion test. (b) left: photograph of HKUST-1 direct grown on nickel foam substrate without PIL; right: photograph of a tape after abrasion test. Compared with the membrane obtained by PIL-assisted replacement method, the green powder can be observed on the tape after peeled off from the HKUST-1 superstructure obtained by direct growth method (b), indicating that HKUST-1 crystals can't tightly bind the substrate.

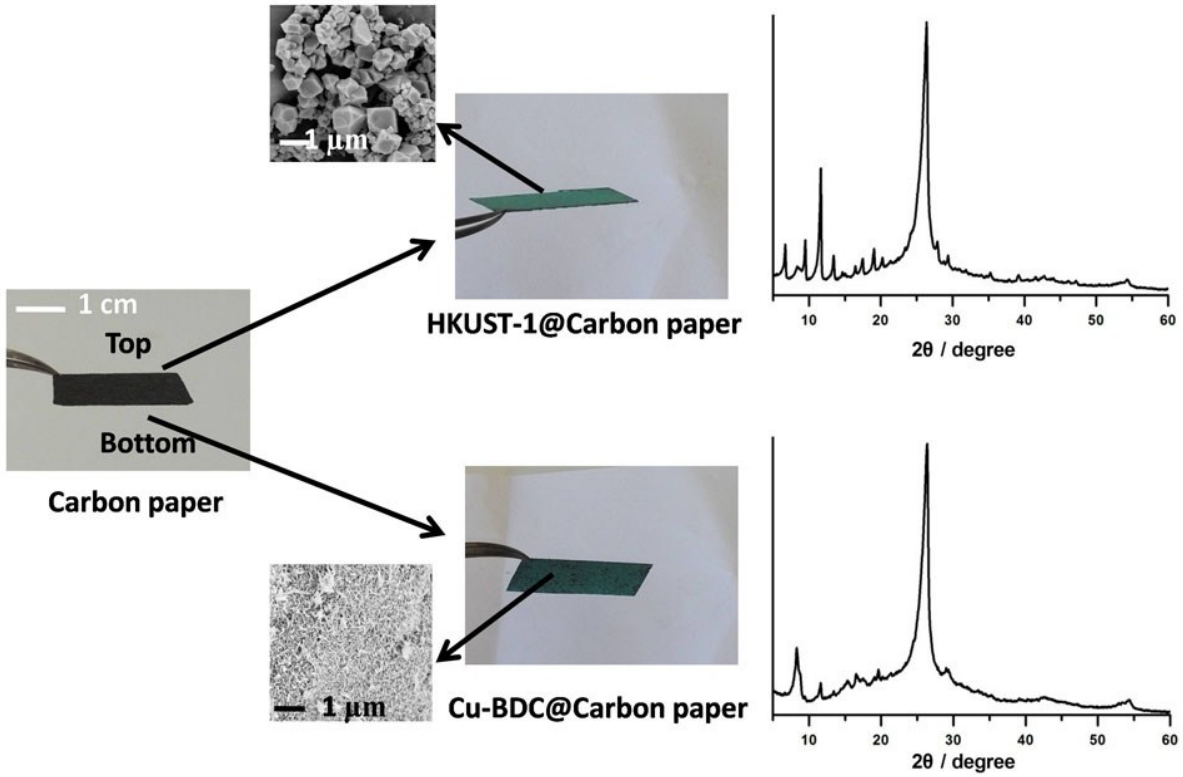

Figure S28. The growth of Janus MOF (HKUST-1 and Cu-BDC) carbon membrane. The successful positioning of the MOF phases on the substrate was demonstrated by XRD patterns and SEM images.

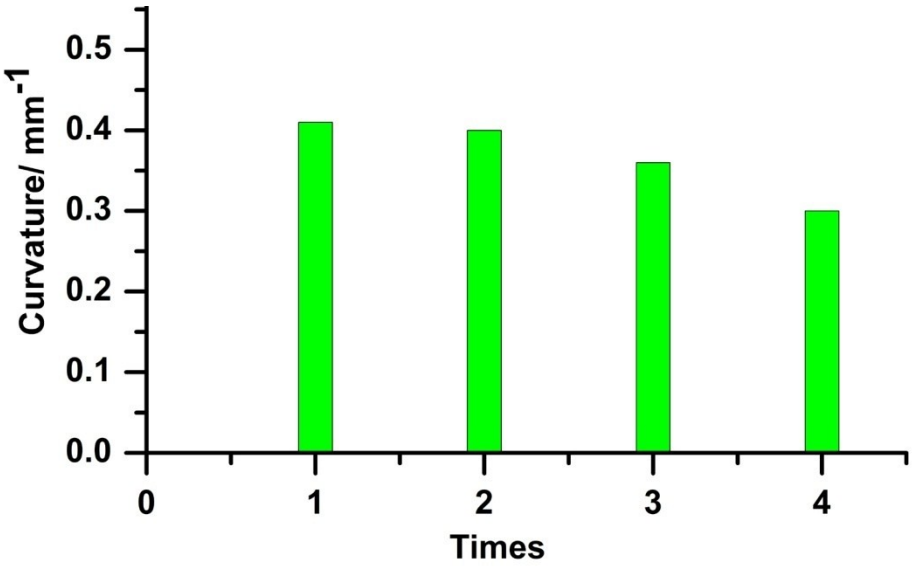

Figure S29. Curvature of the HKUST-1 hybrid membrane actuator versus operation times.

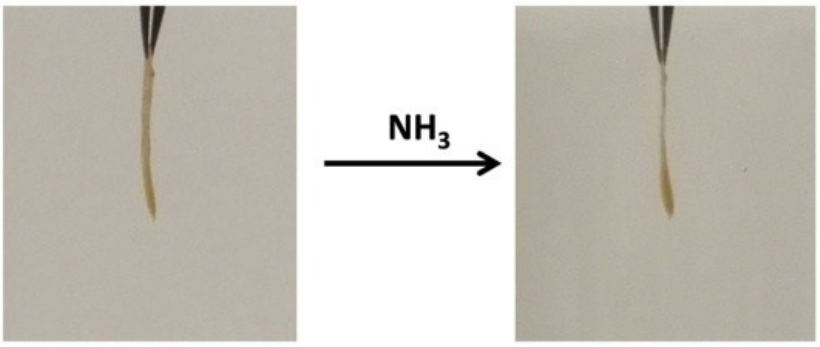

Figure S30. The PIL membrane toward NH_3 gas response. A strip of PIL membrane (13 mm x 2 mm x 35 μm) (left) was directly immersed into NH_3 gas (T = 20 °C, 857 kPa), no obvious movement could be detected (right), indicating that the native PIL membrane can't be actuated by NH_3 gas stimulus.

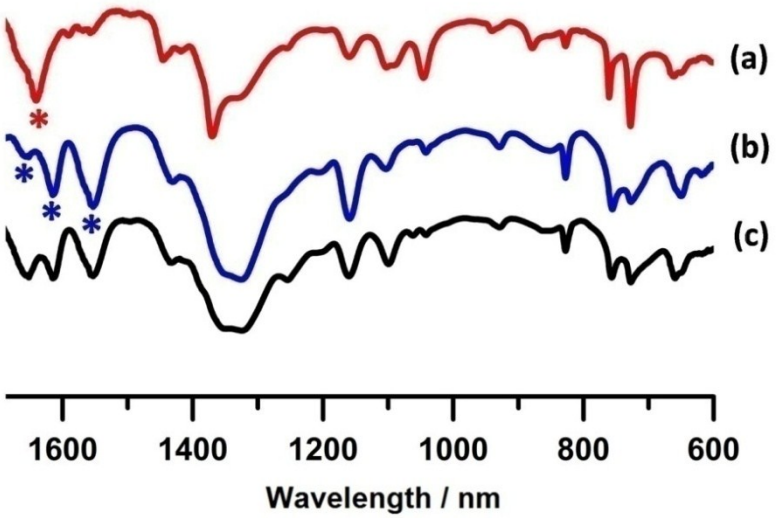

Figure S31. The FT-IR spectra of (a) the as-synthesized HKUST-1 hybrid membrane, (b) HKUST-1 hybrid membrane after exposure to NH_3 gas (denoted as HKUST-1-NH_3 hybrid membrane), (c) the HKUST-1-NH_3 hybrid membrane after heat-treatment. The spectrum of HKUST-1-NH_3 hybrid membrane (b) indicated that the origin carboxylate band (1643 cm^{-1}, red asterisk) in (a) split into two bands (1654 and 1615 cm^{-1}, blue asterisks), which could be attributed the influence of NH_3 molecule at Cu (II) site on the origin vibration of Cu-carboxylate band. Furthermore, an N–H band at 1556 cm^{-1} (blue asterisk) was detected in the same membrane, indicative of ammonia immobilized in the membrane.[7] It can be seen that upon heating the N–H band at 1556 cm^{-1} decreases, indicating the leaving of partial NH_3 molecules from the membrane. Meanwhile, the band at 1654 cm^{-1}, which can be assigned to the Cu-carboxylate band, recovers its intensity to some extent, as the Cu ion liberated from the coordination with NH_3 molecule is now coordinating with carboxylate again.

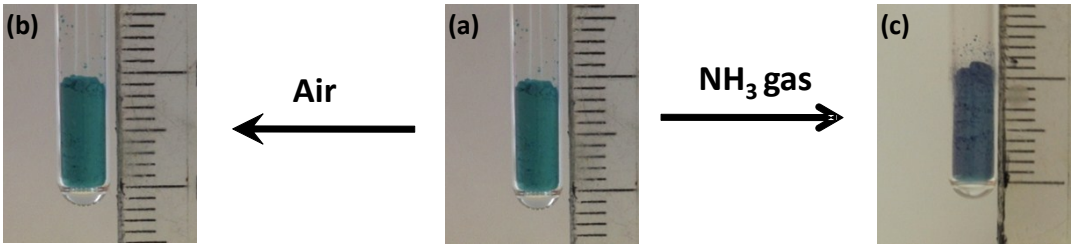

Figure S32. Images of HKUST-1 polycrystalline sample (a in air (b) and NH_3 gas (c), respectively (The scale bar for one grid is 1 mm). An obvious swelling of the sample was observed when placing the HKUST-1 sample in continuous NH_3 gas, the color of the sample changes due to the NH_3 coordinated to the Cu(II) site of HKUST-1, which is consistent with the literature.[8] In comparison, HKUST-1 swells in NH_3 but not in air.

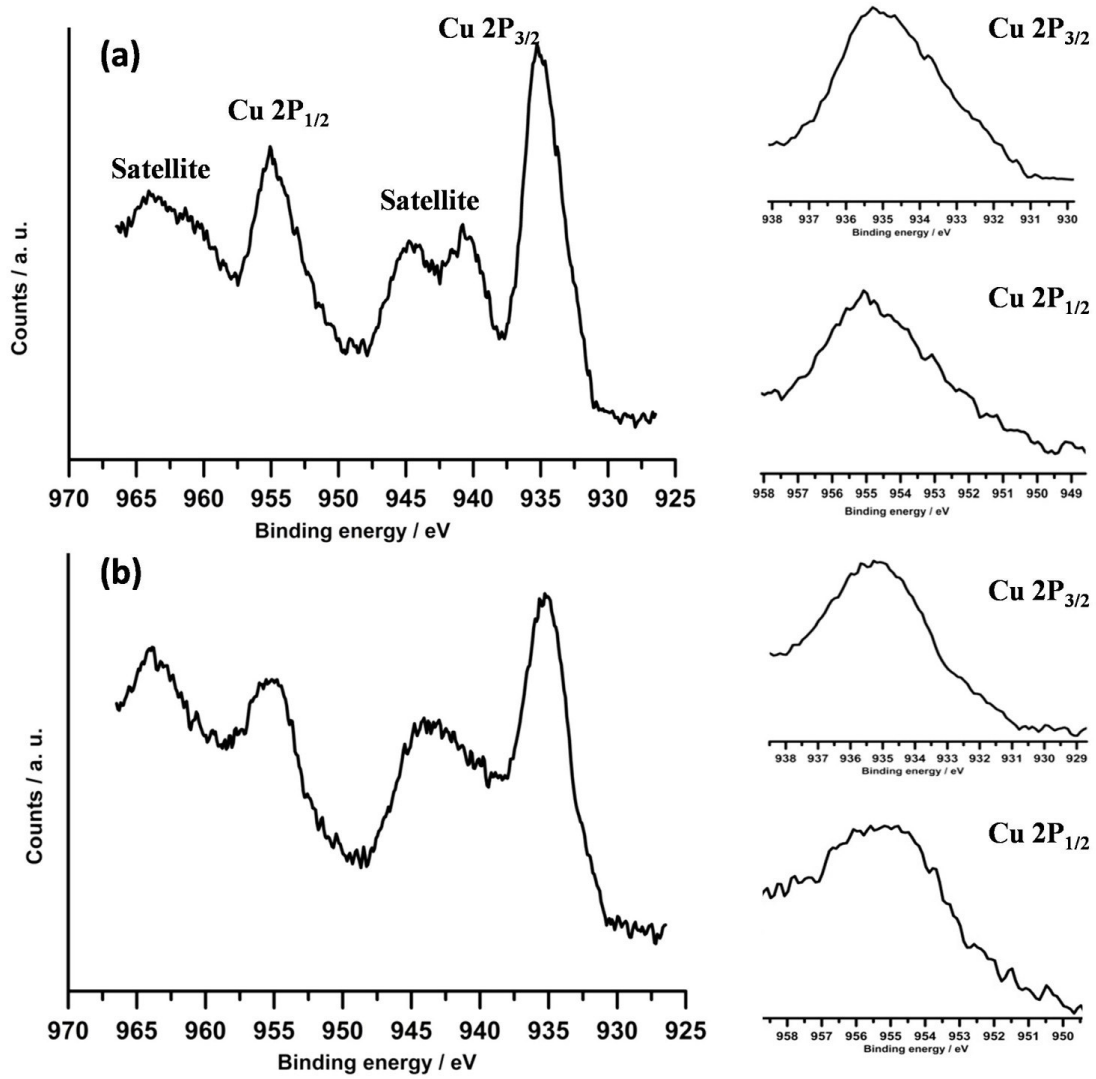

Figure S33. XPS spectroscopy characterizations. Cu 2p signals of top surfaces in (a) HKUST-1 hybrid membrane and (b) HKUST-1-NH_3 hybrid membrane. The right column is an enlarged view of Cu 2p

singles for clarity. A shift of Cu $2P_{3/2}$ and Cu $2P_{1/2}$ peaks to lower binding energy positions from HKUST-1 hybrid membrane (935.3 and 955.1 eV) to HKUST-1-NH_3 hybrid membrane (935.2 and 955.0 eV) could be observed, indicative of interaction of NH_3 with Cu(II) site of HKUST-1 crystals on the top surface of membrane.

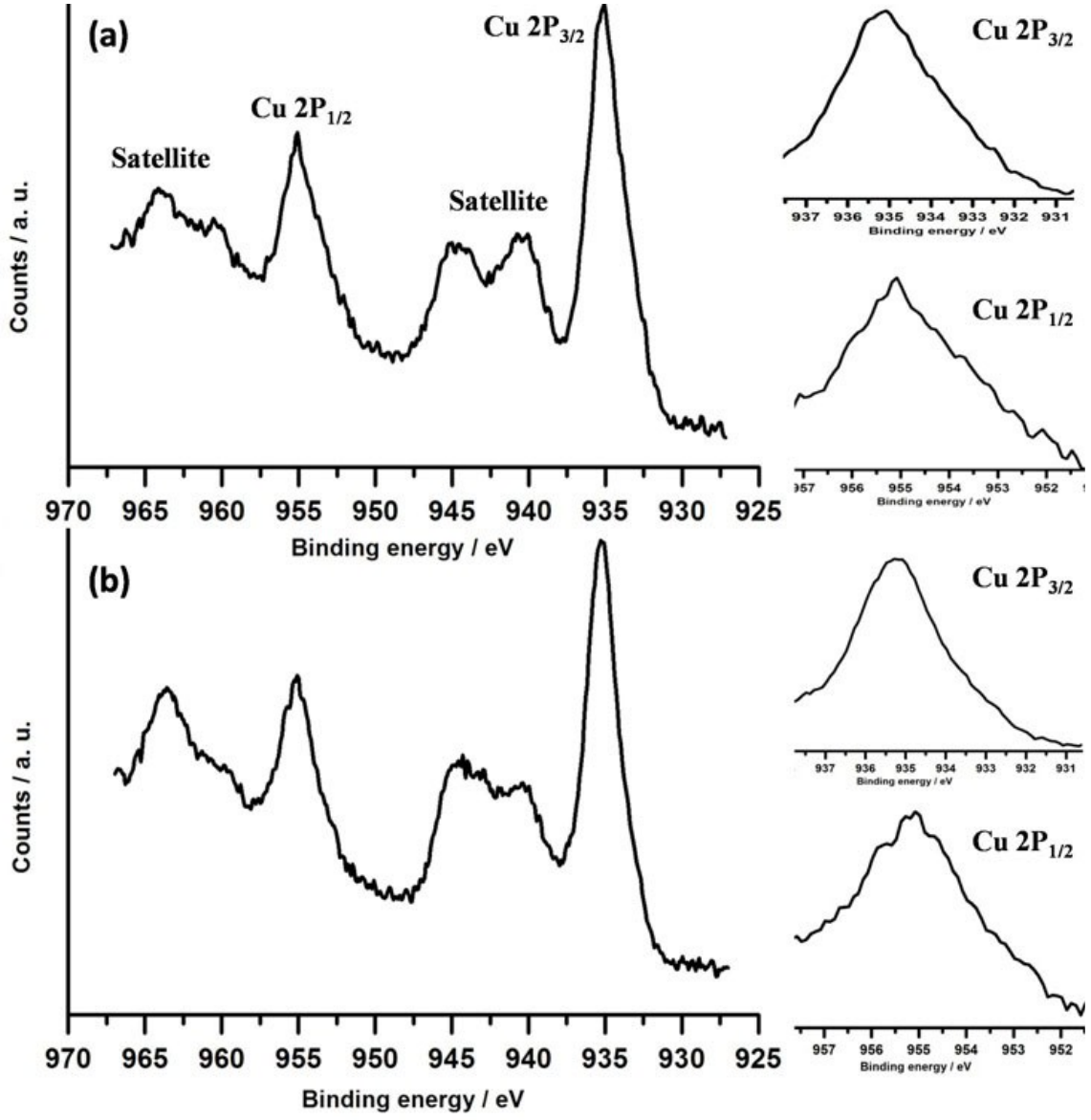

Figure S34. XPS spectroscopy characterizations. Cu 2p signals of bottom surfaces in (a) HKUST-1 hybrid membrane and (b) HKUST-1-NH_3 hybrid membrane. The right column is the enlarged view of Cu 2p signals for clarity. A shift of Cu $2P_{3/2}$ and Cu $2P_{1/2}$ peaks to lower binding energy positions from HKUST-1 hybrid membrane (935.3 and 955.1 eV) to HKUST-1-NH_3 hybrid membrane (934.8 and 954.4 eV) could be observed. Compared with the XPS data of top surfaces (Supplementary Figure 30), we could conclude that

the interaction between NH_3 and Cu(II) site of HKUST-1 crystals on bottom surface of membrane is much stronger than that of top surface.

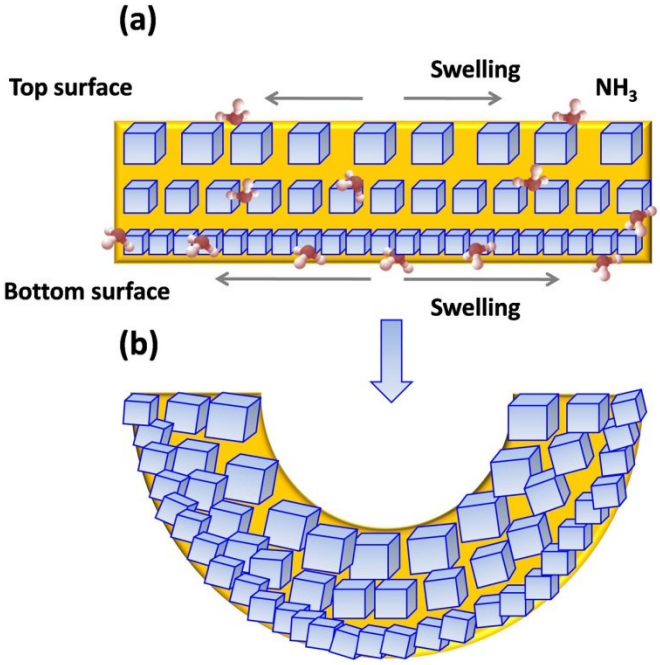

Figure S35. A scheme of the HKUST-1 hybrid membrane actuator (not to scale) toward NH_3 gas response. (a) The HKUST-1 hybrid membrane carries large crystals on the top, but the absolute mass of HKUST-1 crystals is higher at the bottom. It means, the membrane has more HKUST-1 at the bottom, though these crystals are smaller than on the top. (b) The asymmetric swelling strains in the membrane leads to the bending of the membrane with top surface inwards because the volume change due to swelling of crystals at the bottom is more than that on the top.

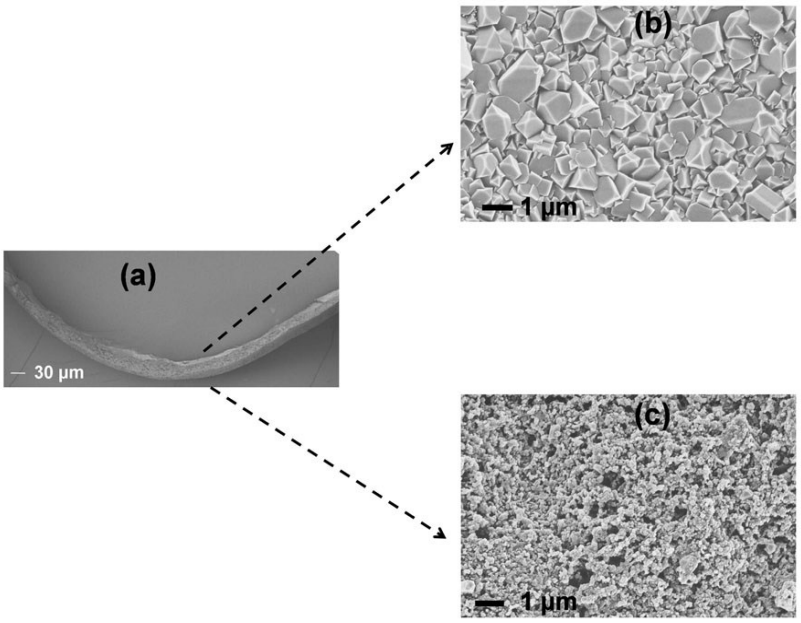

Figure S36. (a) The SEM image of bended HKUST-1 hybrid membrane after exposure to NH_3 gas. (b) front side, (c) back side.

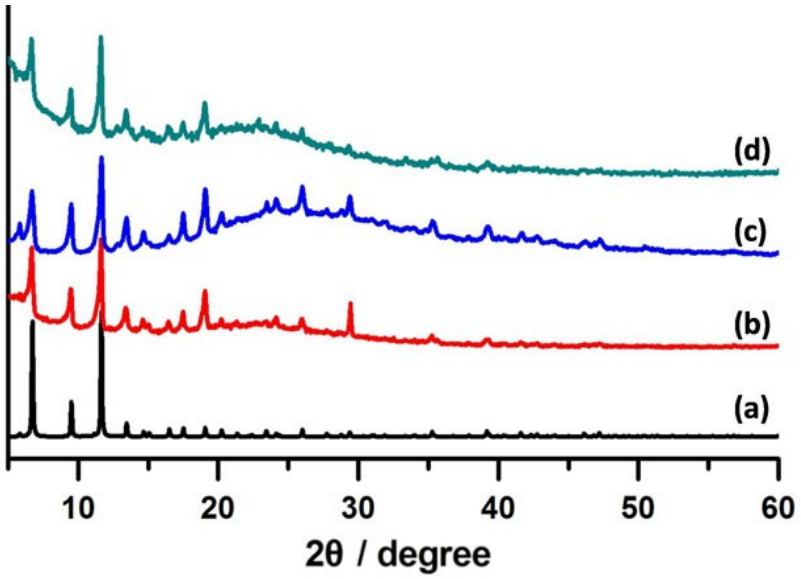

Figure S37. XRD patterns of (a) simulated HKUST-1, (b) as-synthesized HKUST-1 hybrid membrane, (c) HKUST-1 hybrid membrane after exposure to NH_3 gas, (d) after heat-treatment of bended HKUST-1 hybrid membrane.

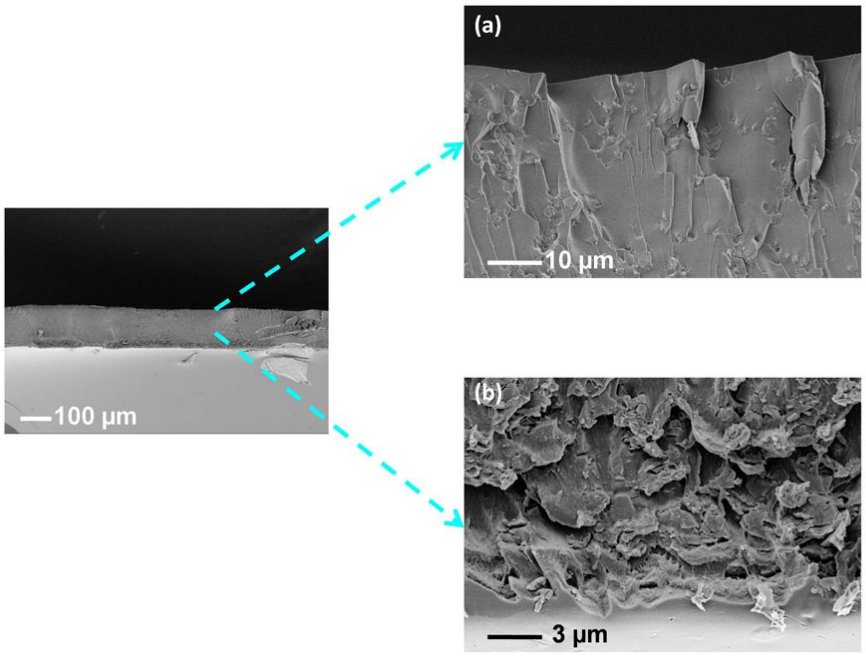

Figure S38. SEM images of HKUST-1 hybrid membrane obtained by direct mixing as-synthesized HKUST-1 crystals with PIL. (a) Upper part view, (b) lower part view.

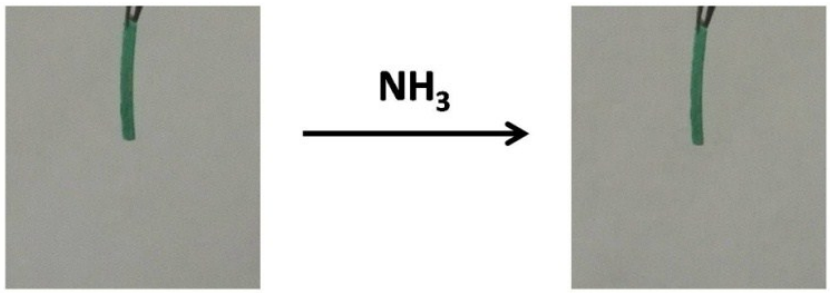

Figure S39. The HKUST-1 hybrid membrane fragment in contact with NH_3 gas. A fragment (11 mm x 2 mm x 48 μm) obtained by direct mixing as-synthesized HKUST-1 crystals with PIL was used here**.** Since there is no gradient in the crystal size and mass content along the cross-section, the volume expansion is even across the whole membrane, thus no actuation is observed.

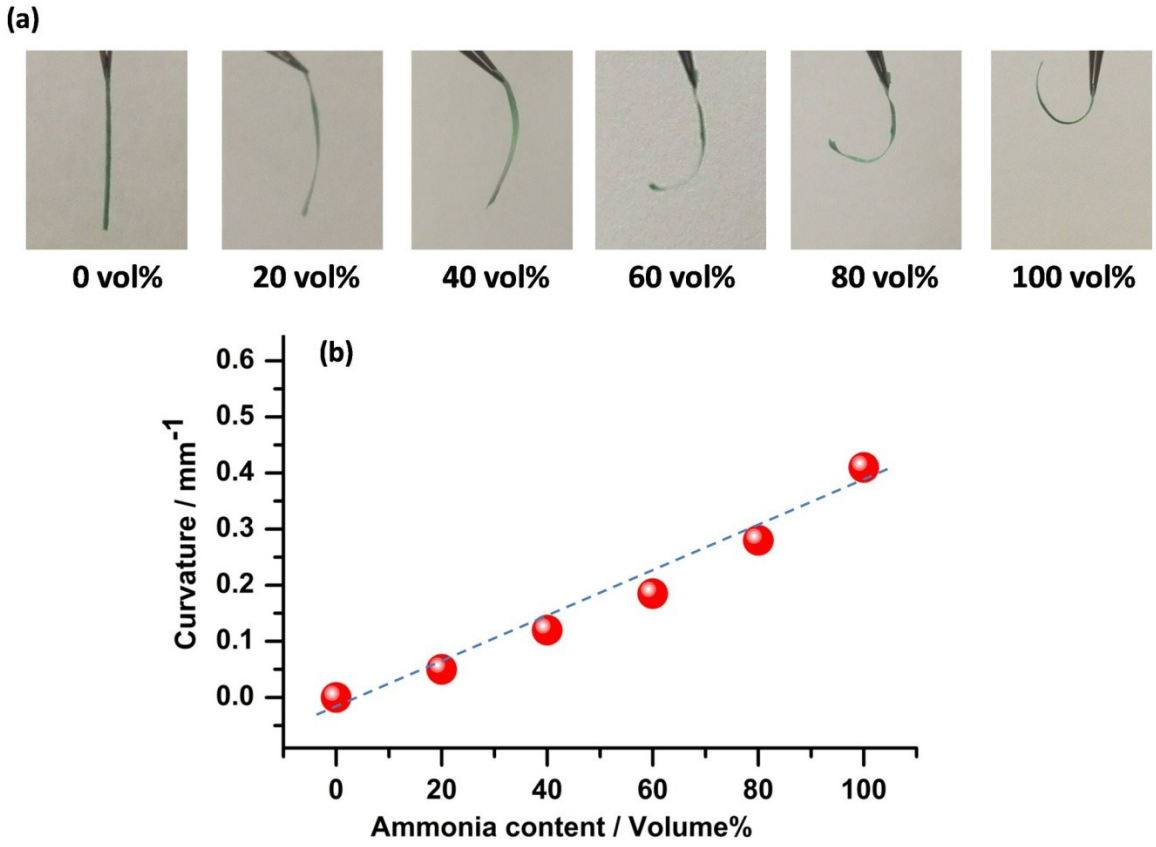

Figure S40. Shape deformation of HKUST-1 hybrid membrane in response to the NH_3 gas. (a) A freshly prepared HKUST-1 hybrid membrane (11 mm × 2 mm × 38 μm) was put into the NH_3 gas at different volume concentration in air (vol%) at 20 °C. (b) Plot of curvature (mm^{-1}) of the HKUST-1 hybrid membrane actuator against NH_3 gas concentration in air.

Table S1. The selected prototypical soft actuators toward external stimuli. The materials with one way bending movements are considered.

Type of actuator	**Type of stimulus**	**Actuator Thickness (mm)**	**Curvature (mm^{-1})**	**Curvature × thickness**	**Time (s)**	**Ref**
Microporous conjugated polymer film	Humidity	0.029	0.48309	0.01401	1.5	9
Polymer/aluminum hybrid film	Humidity	0.003	0.48544	0.00146	56	10
Copolymer film	Light irradiation	0.02	0.16667	0.00333	4.5	11
Cocrystal	Light irradiation	0.01	0.17544	0.00175	3	12
Liquid-crystal polymers	Light irradiation	0.02	0.22936	0.00459	1	13
liquid-crystal polymers	Light irradiation	0.05	0.03472	0.00174	1	14
Ionic liquids /carbon nanotubes	Electric potential	0.02	0.27778	0.00556	1	15
Ionic polymer Membrane	Electric potential	0.127	0.0813	0.01033	30	16
Graphene film	Electric potential	0.05	0.02	0.001	50	17
Grapheme/polymer hybrid	Electric potential	0.1	0.011	0.00011	5	18
Polymer nanofibers	Acid-base	0.03	0.49505	0.01485	20	19
Polymer electrolytes	Electric potential	0.056	0.15924	0.00892	120	20
Wax/nanotube hybrid film	Photothermal	0.023	0.0872	0.002	0.87	21
MOF hybrid membrane	**Ammonia gas**	**0.038**	**0.42**	**0.01596**	**0.5**	**Current work**

3. Information to movies

Supplementary Movie 1

Adaptive movement of a HKUST-1 hybrid membrane (11 mm × 2 mm × 38 μm) when placed in NH_3 gas (T = 20 ^oC, 857 kPa).

Supplementary Movie 2

Unbending NH_3 gas actuated HKUST-1 hybrid membrane when placed in an oven at 80 ^oC. Additional light source was used with the purpose to take the clear video in the oven.

4. References

1. J. Yuan, C. Giordano and M. Antonietti, *Chem. Mater.,* 2010, **22**, 5003-5012.
2. K. Täuber, Q. Zhao, M. Antonietti and J. Yuan, *ACS Macro Lett.,* 2015, **4**, 39-42.
3. Z. F. Ju, Q. X. Yao, W. Wu and J. Zhang, *Dalton Trans.,* 2008, 355-362.
4. H. K. Kim, W. S. Yun, M. B. Kim, J. Y. Kim, Y. S. Bae, J. Lee and N. C. Jeong, *J. Am. Chem. Soc.,* 2015, **137**, 10009-10015.
5. Z. Chen, S. Xiang, D. Zhao and B. Chen, *Cryst. Growth Des.,* 2009, **9**, 5293-5296.
6. C. G. Carson, K. Hardcastle, J. Schwartz, X. Liu, C. Hoffmann, R. A. Gerhardt and R. Tannenbaum. *Eur. J. Inorg. Chem.,* 2009, 2338-2343.
7. J. B. DeCoste, M. S. Denny, Jr., G. W. Peterson, J. J. Mahle and S. M. Cohen, *Chem. Sci.,* 2016, **7**, 2711-2716.
8. E. Borfecchia, S. Maurelli, D. Gianolio, E. Groppo, M. Chiesa, F. Bonino and C. Lamberti, *J. Phys. Chem. C* 2012, **116**, 19839-19850.
9. W. E. Lee, Y. J. Jin, L. S. Park and G. Kwak, *Adv. Mater.*, 2012, **24**, 5604-5609.
10. Y. Ma and J. Sun, *Chem. Mater.,* 2009, **21**, 898-902.
11. Y. Jin, S. I. M. Paris and J. J. Rack, *Adv. Mater.,* 2011, **23**, 4312-4317.
12. M. Morimoto and M. Irie, *J. Am. Chem. Soc.,* 2010, **132**, 14172-14178.
13. W. Wu, L. Yao, T. Yang, R. Yin, F. Li and Y. Yu, *J. Am. Chem. Soc.,* 2011, **133**, 15810-15813.
14. K. M. Lee, D. H. Wang, H. Koerner, R. A. Vaia, L. S. Tan and T. J. White, *Angew. Chem. Int. Ed.*, 2012, **51**, 4117-4121.
15. K. Mukai, K. Asaka, T. Sugino, K. Kiyohara, I. Takeuchi, N. Terasawa, D. N. Futaba, K. Hata, T. Fukushima and T. Aida, *Adv. Mater.,* 2009*,* **21**, 1582-1585.
16. J. Lu, S. G. Kim, S. Lee and I. K. Oh, *Adv. Funct. Mater.,* 2008, **18**, 1290-1298.
17. X. Xie, L. Qu, C. Zhou, Y. Li, J. Zhu, H. Bai, G. Shi and L. Dai, *ACS Nano* 2010, **4**, 6050-6054.
18. J. Liang, L. Huang, N. Li, Y. Huang, Y. Wu, S. Fang, J. Oh, M. Kozlov, Y. Ma, F. Li, R. Baughman and Y. Chen, *ACS Nano* 2012, **6**, 4508-4519.
19. C. O. Baker, B. Shedd, P. C. Innis, P. G. Whitten, G. M. Spinks, G. G. Wallace and R. B. Kaner, *Adv. Mater.,* 2008*,* **20**, 155-158.
20. O. Kim, T. J. Shin and M. J. Park, *Nat. Commun.,* 2013, **4**, 2208.
21. J. Deng, J. Li, P. Chen, X. Fang, X. Sun, Y. Jiang, W. Weng, B. Wang and H. Peng, *J. Am. Chem. Soc.,* 2016, **138**, 225-230.